8-2016

The effect of static and dynamic aging on fatigue behavior of Sn3.0Ag0.5Cu solder alloy

Yiran Li
Purdue University

Graduate School Form
30 Updated 12/26/2015

PURDUE UNIVERSITY
GRADUATE SCHOOL
Thesis/Dissertation Acceptance

This is to certify that the thesis/dissertation prepared

By Yiran Li

Entitled

THE EFFECT OF STATIC AND DYNAMIC AGING ON FATIGUE BEHAVIOR OF SN3.0AG0.5CU SOLDER ALLOY

For the degree of Master of Science in Mechanical Engineering

Is approved by the final examining committee:

Ganesh Subbarayan-Shastri Chair	
Marisol Koslowski	
Weinong W. Chen	

To the best of my knowledge and as understood by the student in the Thesis/Dissertation Agreement, Publication Delay, and Certification Disclaimer (Graduate School Form 32), this thesis/dissertation adheres to the provisions of Purdue University's "Policy of Integrity in Research" and the use of copyright material.

Approved by Major Professor(s): Ganesh Subbarayan-Shastri

Approved by: Jay P. Gore 7/14/2016

Head of the Departmental Graduate Program Date

THE EFFECT OF STATIC AND DYNAMIC AGING ON FATIGUE BEHAVIOR OF SN3.0AG0.5CU SOLDER ALLOY

A Thesis

Submitted to the Faculty

of

Purdue University

by

Yiran Li

In Partial Fulfillment of the

Requirements for the Degree

of

Master of Science in Mechanical Engineering

August 2016

Purdue University

West Lafayette, Indiana

ACKNOWLEDGMENTS

I would like to sincerely thank my advisor Prof. Ganesh Subbarayan for his guidance and support. I feel very fortunate to have such a great mentor who always cares my academic and professional growth. I also want to thank my other committee members: Prof. Weinong Chen and Prof. Marisol Koslowski.

To my past and present labmates (Yuvraj Singh, Dennis Chan, Chaitra Chavali, Anirudh Udupa, Tao Song, Chun-Pei Chen, Pavan Vaitheeswaran, Travis Dale, Maryam Parsa and Prof. Yangjian Xu), I learned a lot from our discussions. Especially, I appreciate the technical assistance from Yuvraj Singh.

Last but not least, my parents are always with me no matter where I am. I am very grateful to them.

TABLE OF CONTENTS

LIST OF TABLES

LIST OF FIGURES

Figure Page

Figure Page

ABSTRACT

Li, Yiran M.S.M.E., Purdue University, August 2016. The Effect of Static and Dynamic Aging on Fatigue Behavior of Sn3.0Ag0.5Cu Solder Alloy. Major Professor: Ganesh Subbarayan, School of Mechanical Engineering.

In microelectronic assemblies, solder joints serve as interconnection between different packaging levels and are an important cause for the failure of microelectronic products. Sn-Ag-Cu solder alloys became important after lead-based solder alloys were caused to be discarded by regulations in European Union and Japan. However, the constitutive behavior of Sn-Ag-Cu alloys is not as well understood as lead-based solder alloys, and many studies confirm the aging of these alloys with time. The aging of Sn-Ag-Cu alloys and its effect on mechanical behavior challenges the reliability prediction of microelectronic assemblies. In this study, the effect of pretest isothermal aging and in-test aging on the fatigue behavior of Sn3.0Ag0.5Cu alloy are examined using the microstructurally adaptive creep model (MACM) and the maximum entropy fracture model (MEFM).

In this thesis, first, the development of microstructurally adaptive creep model is reviewed. Compared to traditional constitutive models, this model considers the effect of thermal history. Two microstructural parameters, the average Ag_3Sn particles size and the average primary-Sn cell size are identified as critical parameters and incorporated into a modified Dorn creep form, which can describe both climb-controlled and glide-controlled dislocation motions.

Next, the maximum entropy fracture model is discussed and compared to traditional fatigue fracture models. The MEFM utilizes the damage accumulation parameter k_ψ, which connects the accumulated damage to the accumulated inelastic dissipation. This parameter is independent of sample geometry, test temperature and strain rate.

Later, using MACM and MEFM, the extraction of the damage accumulation parameters is presented. The creep models for different aging conditions are constructed first based on microstructural characterization. The damage accumulation parameters k_ψ of 25°C and 100°C tests are fit using MEFM. The parameters are presumed different for the two conditions because of the different aging states of the material.

The concepts of static aging and dynamic aging are introduced and utilized to describe pretest aging and in-test aging. In 25°C test, with longer static aging, the k_ψ is smaller, indicating a faster fatigue damage accumulation. Through the relationship between k_ψ and the average primary-Sn cell size $\bar{\eta}$, the influence of microstructural evolution introduced by static aging on fatigue behavior is confirmed. In 100°C tests, the effect of dynamic aging is captured by the change of k_ψ in experiments. Comparing the k_ψ from 25°C and 100°C tests, during test, further aging of Sn3.0Ag0.5Cu microstructure occurs, degrading fatigue behavior until microstructural evolution is completed.

Finally, the thesis is summarized and future work to better characterize the relationship between fatigue behavior and microstructure is put forward. The proposed work includes building a dynamic aging model and microstructural evolution model.

1. INTRODUCTION AND MOTIVATION

1.1 Background

1.1.1 Development of Solder Joint Technology

Solder joint is a critical element in microelectronic assembly because it serves as an interconnection between different packaging levels, providing mechanical and electrical connection. Figure 1.1 shows a schematic of a subassembly in microelectronics, where the solder joints shown in yellow color connect sensor to Printed Circuit Board (PCB). Currently, Surface Mount Technology (SMT) is the dominant assembly technology. There are two main types of Surface Mount Technology (SMT) solder joints: (a) area-array and (b) peripheral array as shown in Figure 1.2 [1].

Due to regulations banning use of Pb in consumer electronics in European Union and Japan, the Pb-based solder alloys have been abandoned because of environmental concern. There are many Sn-based alternative solder alloys with different elements, such as Ag, Cu, Zn, Bi or In. Among these lead-free solder materials, the Sn-Ag-Cu (SAC) alloys have gained popularity in industry because of their advantages in

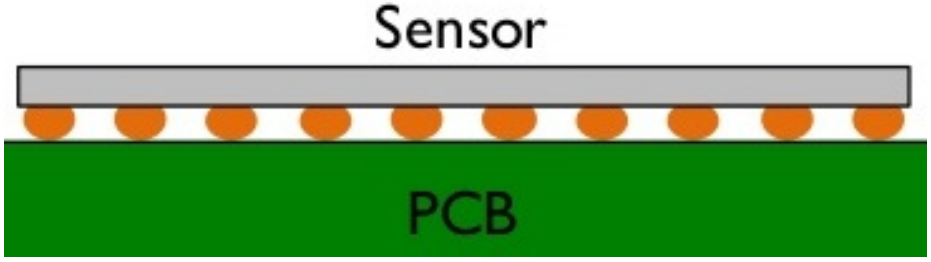

Figure 1.1. Schematic of an assembly cross section showing sensor-solder-PCB subassembly.

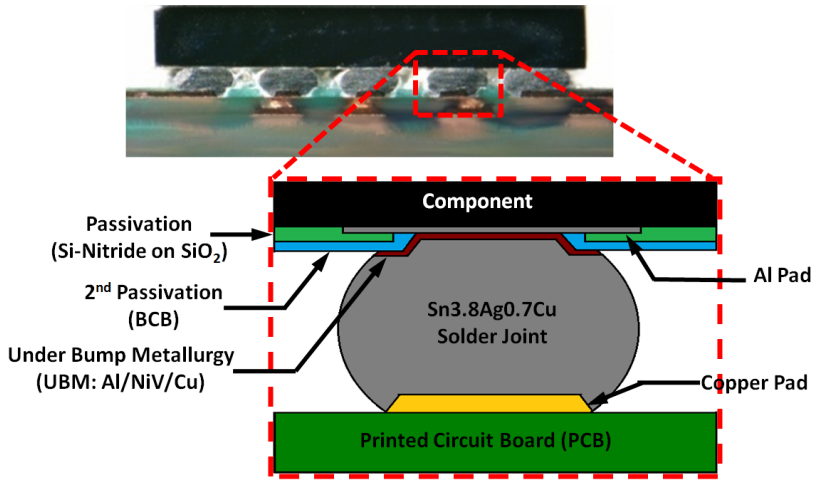

(a)

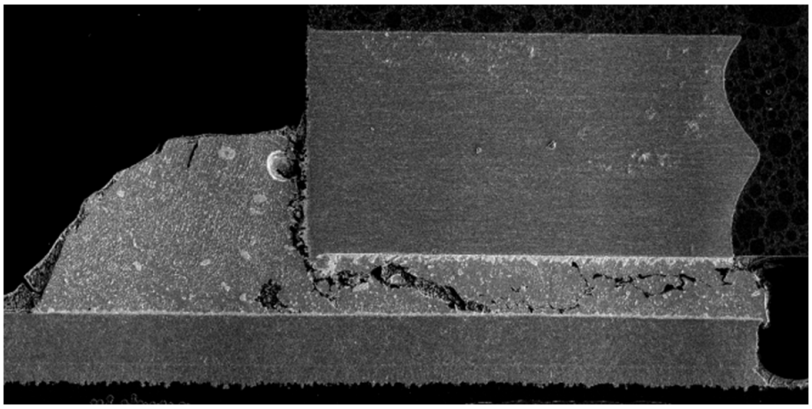

(b)

Figure 1.2. Two main types of Surface Mount Technology solder joints: (a) area-array and (b) peripheral array [1].

manufacturability, cost and reliability [2]. However, the behavior of Sn-Ag-Cu solder alloys is not as well understood at this time as that of Sn-Pb solder alloys.

In addition, with increased chip-level integration, the size of solder joints and the pitch of the solder joints continues to decrease. All of these changes mentioned above challenge the reliability of microelectronics.

1.1.2 Failure of Solder Joints

Typically, the fracture of solder joints is caused by thermomechanical fatigue or impact loading [1]. Office electronic equipment, such as a desktop computer, are susceptible to thermomechanical fatigue. For example, in the assembly shown in Figure 1.1, due to the mismatch in coefficients of thermal expansion between sensor and PCB, the top and bottom sides of solder joints are subject to differing amounts of expansion, which causes the initiation and propagation of fracture during thermal cycling. As for mobile devices, such as laptop or mobile phone, impact loading also becomes an important reliability consideration. Figure 1.3 shows fractures caused by thermomechanical fatigue and impact loading. In this study, we focus on thermomechanical fatigue, where the fracture tends to propagate through the bulk material but very close to the pad interface where intermetallics are formed.

1.2 Motivation

1.2.1 The Influence of Aging on Reliability of SnAgCu Solder Joints

Many studies show that isothermal aging could lead to the degradation of mechanical properties of SnAgCu alloys, such as stiffness and strength [2–5]. This could have a detrimental effect on the reliability of solder joints [3]. Lee et al. [4] studied the relationship between isothermal aging and the reliability of fine-pitch ball grid array (BGA) packages with Sn3.0Ag0.5Cu solder joints during thermal cycling. From Weibull plots, they found that compared to unaged package, the characteristic life-

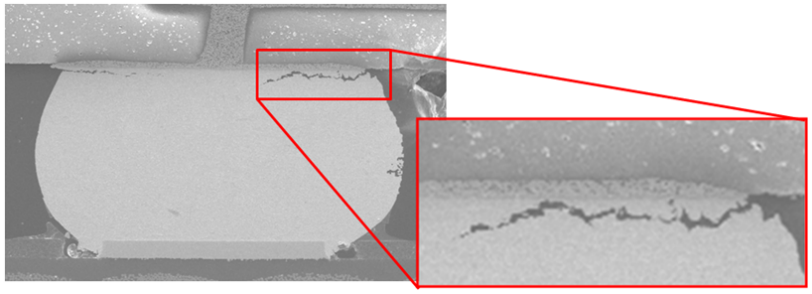

(a)

(b)

Figure 1.3. (a) Fracture caused by thermomechanical fatigue and (b) fracture caused by drop test [1].

time dropped 44% after 1000-hour isothermal aging at 150°C. In another study, Lee et al. [5] studied wafer-level chip-scale packages (WLCSPs) with Sn3.0Ag0.5Cu solder joints and found that the characteristic lifetime dropped 29% after isothermal aging at 150°C for 500 hours. Zhang et al. [2] compared the characteristic lifetime of BGA packages with Sn1.0Ag0.5Cu and Sn3.0Ag0.5Cu solder joints. Three different board finishes and various preconditioning agings before thermal cycling were adopted and all tests indicated that higher aging temperature, longer isothermal aging time lead to greater reduction in solder joint life.

In addition, the aging that happens during accelerated product test could significantly influence the reliability as well. A comprehensive thermal fatigue study was performed by Coyle et al. [6] on various Pb-free solder joint materials. The authors conducted accelerated temperature tests with different dwell time. Strong inverse relationships between dwell time and reliability were observed for all types of Pb-free materials.

1.2.2 Review: Solder Joint Reliability Prediction

Schubert et al. [7] tried to extend the life models of SnPb solder joints to lead-free solder joints by studying flip chip on board (FCOB) and plastic ball grid arrays (PBGA). The author adopted double power law creep equation and hyperbolic sine equation as constitutive models and predicted reliability with strain-based and energy-density based approaches. The reliability predictions fit the experimental results well. However, Syed [8] did similar study and found that the energy-based method yielded a more consistent prediction with different constitutive models than strain-based approach. Zhang et al. [9] used energy-partitioning model to predict the reliability of Sn3.9Ag0.6Cu solder joints in thermomechanical tests. By simulating isothermal cyclic tests with a viscoplastic constitutive model developed from simulations and experiments, the creep energy and plastic work were separated for all testing conditions. Then the energy-partitioning model constants could be calculated from the

creep energy and plastic work. A damage mechanics-based method was put forward by Tang et al. [10], in which the damage was treated as an internal state variable and incorporated into a unified viscoplastic constitutive model. This model was included in ABAQUS and the simulation results were compared to experimental results from BGA packages. Lee et al. [11] compared fourteen solder joint fatigue models systematically and sorted them into six categories: stress-based, plastic strain-based, creep strain-based, energy-based, damage-based and empirical. A fatigue model selection procedure was put forward based on package conditions and computational power.

As mentioned earlier in Section 1.2.1, aging has a strong influence on the reliability of solder joints and therefore, it is essential to include aging effect in fatigue prediction. However, the fatigue prediction methods mentioned above ignore the influence of aging on both constitutive model and failure model. An accurate fatigue prediction method should be able to incorporate the effect of whole thermal history, such as the isothermal aging before fatigue tests and the in-test aging happens during the test.

Recently, Motalab et al. [3] developed a revised set off Anand viscoplastic stress-strain relationships and aging aware failure criteria for Sn3.0Ag0.5Cu alloy. In order to study how aging influences the nine parameters of Anand model, the samples were aged for eight different aging times up to 12 months at 100°C. For each set of aging conditions, uniaxial stress-strain experiments at three different strain rates and five temperatures were performed. More than one thousand tests were conducted and the data of each test was used to fit the Anand viscoplastic model. Seven out of nine parameters were empirically fit as functions of aging time and aging temperature respectively. Following the same idea, the evolution of the constants in Coffin-Manson and Morrow-Darveaux fatigue criteria were identified from thermomechanical tests. Although the effect of aging is incorporated into the revised Anand model empirically, the physical mechanism of aging was not clarified. As for the fatigue models, since the geometrical effect of samples used in the tests is not clear, such time-consuming experiments may be necessary for each type of package.

The Maximum Entropy Fracture Model (MEFM) was developed by Bhate et al. [12] based on information theory and statistical thermodynamics. The author argued that with maximum entropy principle, the reliability prediction becomes possible even when microstructural uncertainties exist. A single damage accumulation parameter independent of strain rate, temperature and sample geometry could be extracted from cyclical fatigue tests. Later, the MEFM was verified by Chan et al. [13] with experiments and simulations on Sn3.8Ag0.7Cu solder joints. In Tucker's study [14], Sn3.8Ag0.7Cu and Sn3.0Ag0.5Cu solder alloys were studied using the MEFM combined with Anand viscoplastic constitutive model. Tucker performed cyclical fatigue tests at different strain rates and temperatures with samples initially under different isothermal aging conditions. Based on their studies, he confirmed that the test temperature has influence on fatigue behavior of SnAgCu alloys, especially the unaged samples. However, further study is required to quantitatively understand the effect of in-test aging.

1.3 Scope of the Thesis

The main research goal of this thesis is adopting a systematic approach to study the effect of isothermal aging prior to test as well as in-test aging on the fatigue behavior of Sn3.0Ag0.5Cu alloy with the Maximum Entropy Fracture Model combined with the Microstructurally Adaptive Creep Model developed by Chavali et al. [15]. The thesis consists of the following parts:

Chapter 2 reviews the Microstructurally Adaptive Creep Model developed by Chavali et al. [15]. This model identifies and incorporates two microstructural features affected by thermal history into a modified Dorn creep form, which could describe both climb-controlled and glide-controlled dislocation motions.

In Chapter 3, key concepts of the Maximum Entropy Fracture Model (MEFM) are covered. The experimental procedure and the extraction method of a single damage accumulation parameter are reviewed.

In Chapter 4 the creep models are constructed for different aging conditions based on microstructural characterization. Then the fatigue test data is processed using MEFM to determine the damage accumulation parameters k_ψ. Because inelastic dissipation pattern in 100°C tests is different from that in 25°C tests, a new equation is derived to calculate k_ψ. The k_ψ values are shown to reduce and reach a steady value asymptotically during 100°C tests, clearly capturing the effect of in-test aging at high temperature.

Chapter 5 focuses on the effect of aging. The concepts of static aging and dynamic aging are clarified and utilized to describe pretest aging and in-test aging. The effect of static aging is revealed from 25°C tests and the relationship between microstructure and k_ψ (fatigue behavior) is presented. In 100°C tests, dynamic aging exists and it could further age samples, degrade fatigue behavior of Sn3.0Ag0.5Cu alloy until microstructure becomes stable.

Finally, in Chapter 6, the work of this study is summarized and some suggestions are put forward for future study.

2. A MICROSTRUCTURALLY ADAPTIVE CREEP MODEL FOR SNAGCU SOLDER ALLOYS

Numerous studies on SnAgCu alloys have shown that the evolution of the microstructural state has a strong influence on the mechanical properties [16,17] such as tensile strength, elastic modulus and fatigue life. However, most models do not quantitatively describe the relationship between mechanical behavior and the microstructural states. Generally, three types of modeling approaches may be used to describe heterogeneous materials such as SnAgCu alloys [15]:

1. Microstructural: estimate macroscopic behavior of materials by modeling the microstructural features such as precipitates, grain boundary and their relationships.

2. Mechanistic: explain macroscopic constitutive law of material from microscopic mechanism but without relating the constitutive model to microstructural parameters.

3. Phenomenological: empirically develop constitutive law of material without including microstructural mechanism.

Recently, a microstructurally adaptive creep model was developed by Chavali et al. [15] for SnAgCu alloys based on forty-eight creep experiments. In this creep model, the stress exponent and normalized threshold stress are connected to two representative microstructural features: the average size of Ag_3Sn intermetallic compound precipitates and the primary-Sn dendrites, which captures the major changes in microstructure under different aging conditions. The author showed that these two microstructural features have close connections to the mechanism of dislocation movement that causes strain in SnAgCu alloys. This model successfully captured

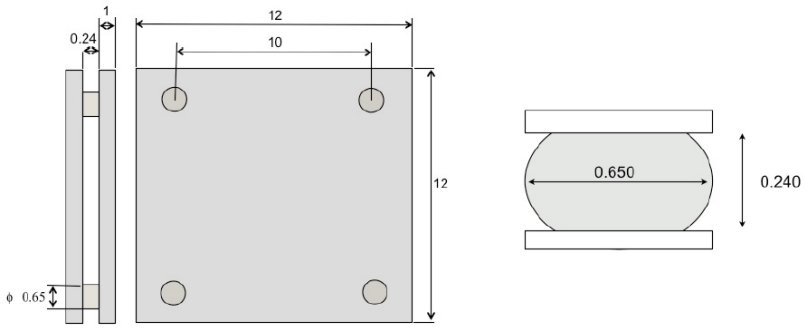

Figure 2.1. Sn3.0Ag0.5Cu solder joints at four corners between two alumina substrates [15].

the creep response of same solder joint under very different aging conditions. In the following sections, the major concepts of microstructurally adaptive creep model are reviewed. More details are covered in [15].

2.1 Microstructural Features

In [15], Chavali proposed that $\bar{d}$, the average size of Ag_3Sn particles and $\bar{\eta}$, the average size of primary-Sn dendrites as two key microstructural features based on observations on the evolution of the microstructure. First, the author performed static aging experiments on Sn3.0Ag0.5Cu solder joint samples as shown in Figure 2.1. Four solder joints at corners between two alumina substrates. The samples were aged at 25°C, 75°C and 100°C for varying time. Prior to aging, the samples were stored in a fridge at -10°C to minimize aging. Table 2.1 shows the test matrix.

After static aging, the samples were saturated in a cold resin and solidified. Then they were polished according to standard metallographic techniques. This procedure exposes the microstructure of solder joints and makes it ready for observation. Later scanning electron microscope (SEM) was used to observe microstructure evolution of Sn3.0Ag0.5Cu solder joints over a wide range of static aging conditions. The microstructure of different aging conditions are shown in Figure 2.2. In these images, the shiny particles are Ag_3Sn precipitates and the dark background region is primary-

Table 2.1. Test matrix of static aging of Sn3.0Ag0.5Cu solder alloy [15].

Aging Temp	Short Term Aging	Long Term Aging
	Aging Time (Days)	Aging Time (Days)
25C	1	15
		30
	5	60
		90
75C	1	15
		30
	5	60
		90
125C	1	15
		30
	5	60
		90

Sn dendrites. The network of eutectic region is surrounding the primary-Sn dendrites. Two noticeable trends of microstructural evolution were captured [15]: (a) Ag_3Sn particles grow larger. (b) The network of eutectic microconstituent disintegrates with concurrent increase in the primary-Sn cell size. The network disintegrated clearly at

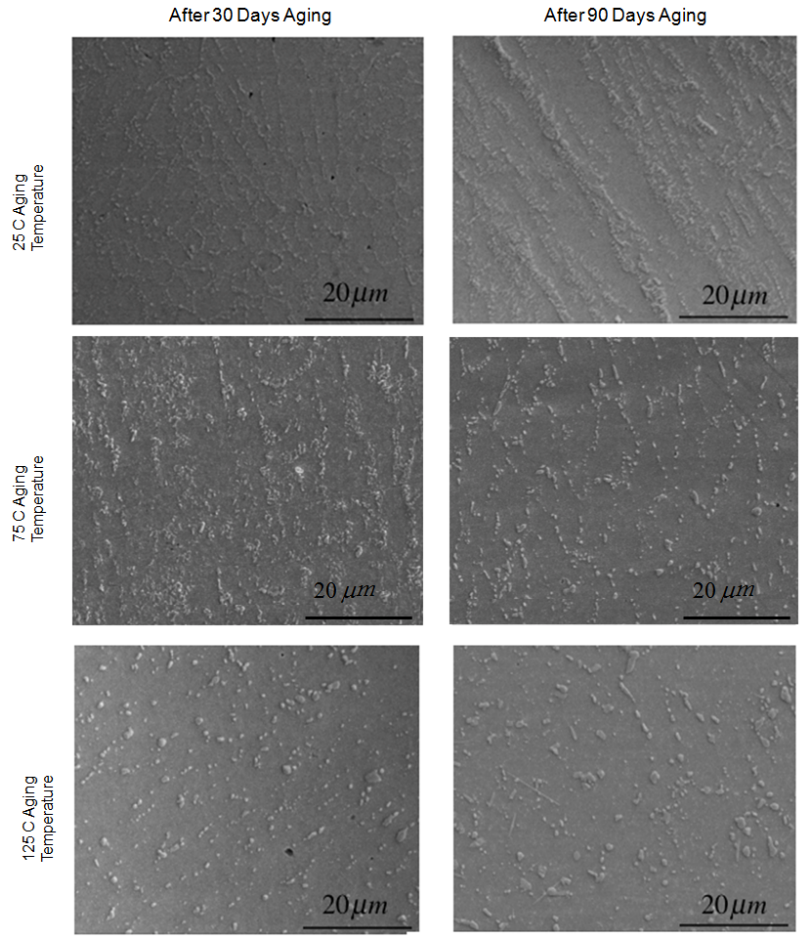

Figure 2.2. Microstructural evolution of Sn3.0Ag0.5Cu solder joints under different aging conditions [15].

75°C and 125°C. However, at 25°C, the network was still visible even after 90-day aging. The Ag_3Sn precipitates significantly coarsen at 125°C compared with 75°C and 25°C.

The flow behavior, or the strain rate of a material is always obstacle limited. In SnAgCu alloys, Ag_3Sn precipitates are strong particles (obstacles) that could affect

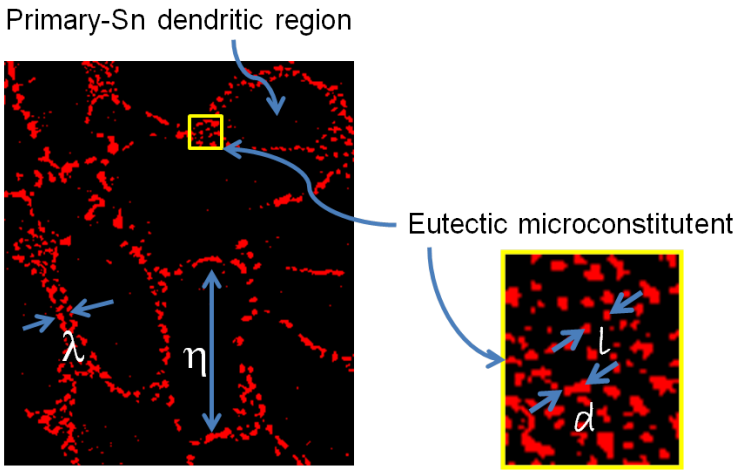

Figure 2.3. The network of eutectic region surrounding the primary-Sn dendrites [15].

the glide and climb processes of dislocation movement [15]. The glide that happens in the Sn matrix between Ag_3Sn particles causes most of the deformation because dislocation bypasses or cuts through the obstacles. In Figure 2.3, the average size of primary-Sn dendrites is denoted by $\bar{\eta}$, which reflects the degree of disintegration of eutectic network and determines the maximum strain within material. The climb process means that the dislocation movement gains another degree of freedom to climb strong precipitates, which has influence on the velocity of dislocation. The climb process is affected by the average size of strong particles, denoted by $\bar{d}$. Therefore, Chavali et al. [15] identified these two measurable microstructural features, which determine the glide and climb processes of dislocation movement hence affect flow behavior of SnAgCu alloy, as the indicators of microstructural evolution due to static aging. These two microstructural indicators are measured using linear stereological method and the results for different static aging conditions are shown in Table 2.2. More details are covered in [15].

Table 2.2. The average particles size of Ag_3Sn and the average size of primary-Sn dendrites under different static aging conditions [15].

Aging Temp	Aging Time (Days)	Ag3Sn Particle Size (um)	Primary-Sn cell szie (um)
-	0	0.52	6.50
25C	15	0.65	6.62
	30	0.69	6.78
	60	0.71	6.95
	90	0.72	7.17
75C	15	0.71	8.37
	30	0.75	9.64
	60	0.80	10.83
	90	0.88	10.95
125C	15	0.95	11.70
	30	1.01	11.93
	60	1.20	12.50
	90	1.20	12.91

Table 2.3. Test temperature, applied load, aging time and aging temperature in the forty-eight creep tests [15].

Alloy	Test Temp	Applied Load (Mpa)	Aging Time (Days)	Aging Temp
Sn3.0Ag0.5Cu	25C to 125C	13.04 to 45.67	15 to 90	25C to 125C

2.2 Creep Experiments and the Influence of Aging on Creep Behavior

2.2.1 The Double Lap Shear Creep Tests

Forty-eight creep tests were performed by Chavali et al. [15] at various test temperatures with samples under different aging conditions. These tests were carefully designed in order to build a microstructurally adaptive creep model over a wide range of aging conditions while minimizing the number of creep tests. The variable factors in these tests are shown in Table 2.3. The Sn3.0Ag0.5Cu solder joint samples were of the same design as those used in microstructural observation in Section 2.1. A double lap shear configuration was adopted to perform creep tests as shown in Figure 2.4. Two samples with eight solder joints in total were sheared in each creep experiment. This is important because SnAgCu solder joint contains very few Sn grains, and therefore, testing an assembly consisting of many joints yields a different response than testing a single joint. The solder joints have a specific aspect ratio as shown in Figure 2.1 (Aspect Ratio $= \frac{Height\ of\ Solder\ Joint}{Pad\ Diameter} = 0.37$). This special design could achieve a near homogeneous stress state in the solder joint and simplify the calculation for equivalent stress/strain. The sample design is fully discussed in [18].

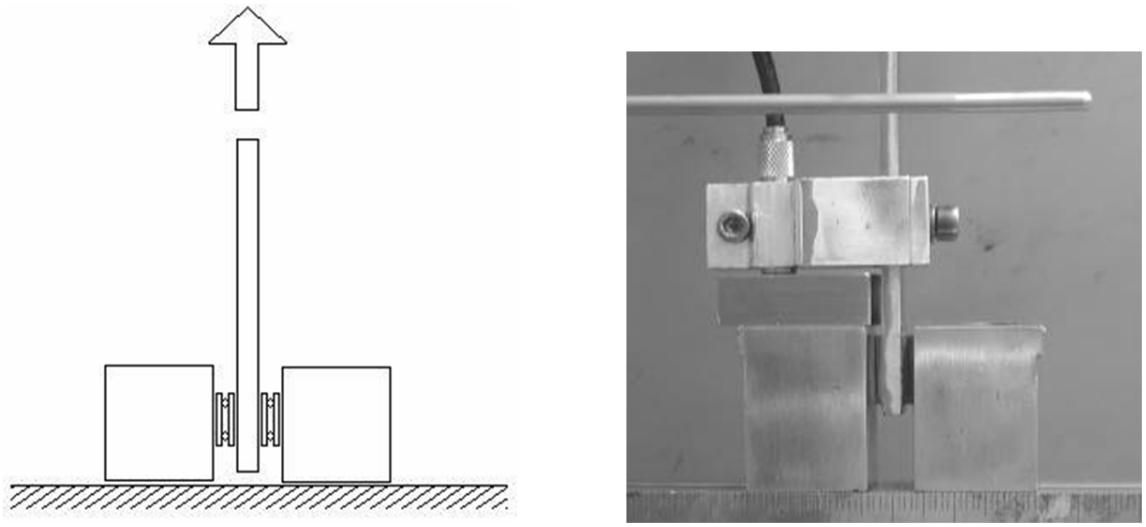

Figure 2.4. (a) Schematic of double lap shear test configuration. (b) A capacitance sensor placed closed to test specimen to minimize compliance in load train [18].

2.2.2 Basic Observations on the Influence of Aging on Creep Behavior

As shown in Figure 2.2, the Ag_3Sn precipitates coarsen and disperse to become a more stable state as aging condition becomes more severe (longer aging time, higher aging temperature). This microstructural evolution leads to increase in the steady-state creep strain rate as shown in Figure 2.5. As for the primary creep of aged samples, it happens over a large portion of total time (about $20 - 40\%$) in creep tests and therefore it is an important part of overall creep behavior. Figure 2.6 indicates that aging could significantly increase primary creep and therefore needs to be considered in the microstructurally adaptive creep model.

Before the effect of aging on creep behavior of unaged samples is examined, the Zener-Hollomon parameter, Z_p, is introduced, which is the temperature compensated strain rate defined as follows [19]:

$$Z_p = A(\frac{\sigma}{E})^n = \dot{\epsilon_{ss}} e^{Q/RT} \tag{2.1}$$

where A is the Dorn proportionality constant, E is Young's modulus, n is stress exponent, $\dot{\epsilon_{ss}}$ is minimum creep strain rate from modified Dorn equation, Q is activation

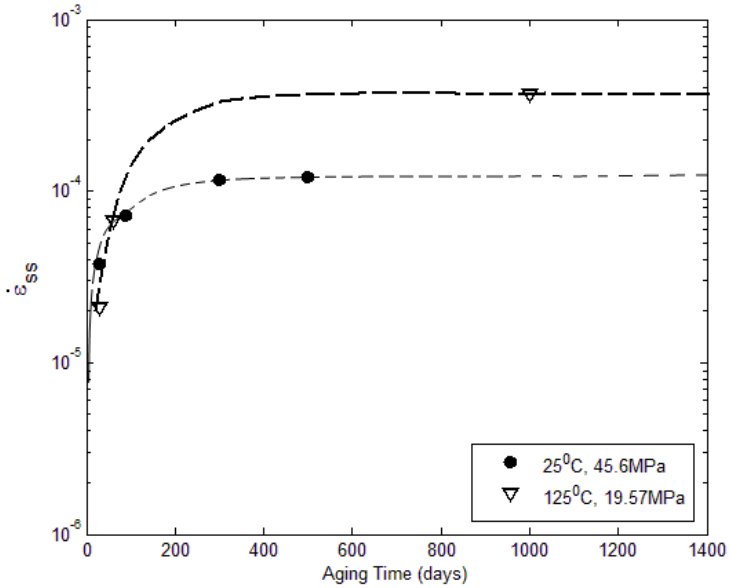

Figure 2.5. Relationship between minimum creep strain rate and aging time at 25°C and 125°C aging temperatures [15].

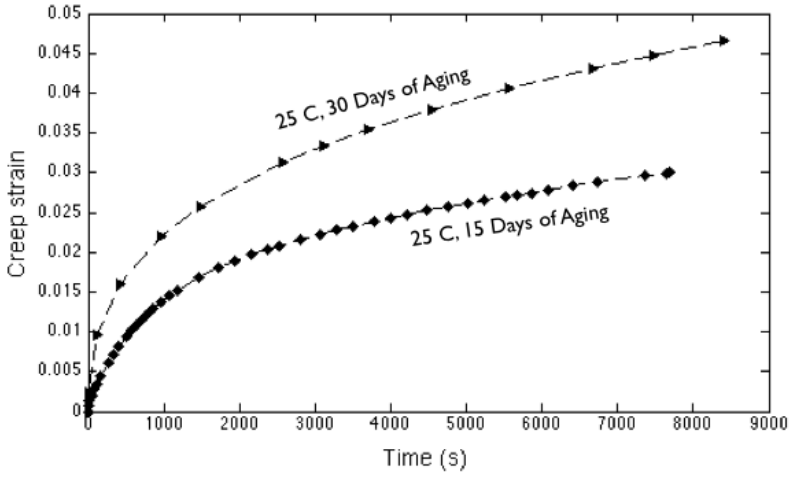

Figure 2.6. The effect of aging on primary creep of Sn3.0Ag0.5Cu solder alloy. Applied stress is 45.6 MPa at 25°C [15].

energy, R is universal gas constant and T is absolute temperature. E is a function of absolute temperature T, as $E = E_0 - 37.97 * (T - 273)$, where E_0 is the Young's modulus of Sn3.0Ag0.5Cu alloy at 0°C. The Zener-Hollomon parameter describes the relationship between dislocation generation and annihilation in creep test. While applied stress generates new dislocations, temperature could annihilate dislocations. From the unaged creep tests, two regimes of Zener-Hollomon parameters were observed by Chavali et al. [15] because of the range of applied stress in creep tests. In Figure 2.7, the transition of Zener-Hollomon parameter indicates the change from glide-controlled dislocation to climb-controlled dislocation. From Figure 2.7, the normalized threshold stress, $\frac{1}{\alpha}$, could be calculated by extracting the x-intercept from the knee and thus the normalized stress coefficient, α, is obtained.

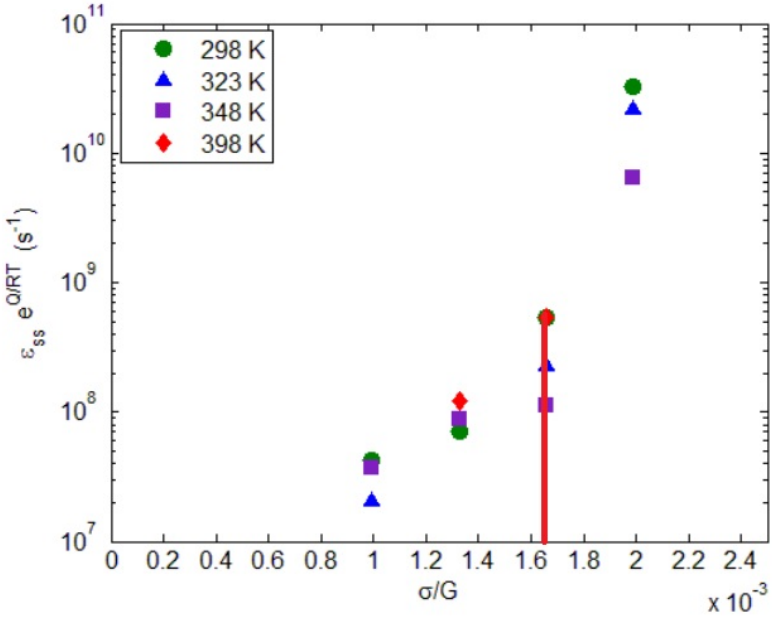

Figure 2.7. Zener-Hollomon parameter vs. normalized saturation stress for unaged Sn3.0Ag0.5Cu solder joints [15].

2.3 A Unified Creep Model Related to Microstructural Parameters

In this section, an exponential time-primary-cum-secondary creep model based on modified Dorn creep form was developed from the creep test data. The stress exponent and the normalized threshold stress were connected to two microstructural parameters respectively, $\bar{d}$ and $\bar{\eta}$ identified in Section 2.1 and therefore, a microstructurally adaptive creep model was completed.

2.3.1 A Unified Creep Model

It is a common phenomenon that soft materials (such as Sn, Al, etc.) reach a steady strain rate after dislocation rearranges itself at an applied stress [20, 21]. Typically, this "normal transient" is described as time hardening or strain hardening with the follows forms:

$$Time\ Hardening : \dot{\epsilon} \propto \frac{\sigma^n}{t^p} \tag{2.2}$$

$$Strain\ Hardening : \dot{\epsilon} \propto \frac{\sigma^n}{\epsilon^{p'}} \tag{2.3}$$

However, both of them predict an infinite strain rate at the beginning of creep. Dorn et al. [20, 21] put forward a creep form that solves this problem.

$$\epsilon = \epsilon_t(1 - e^{-k\dot{\epsilon_{ss}}t}) + \dot{\epsilon_{ss}}t \tag{2.4}$$

where $\dot{\epsilon_{ss}}$ is the minimum creep strain rate, ϵ_t is the total primary creep strain, k is a time constant defined as $k = \frac{E}{\sigma}$.

In Section 2.2.2, the Zener-Hollomon parameter was put forward and two regimes of the Zener-Hollomon parameters was observed from unaged samples. These two regimes indicated the transition between glide-controlled dislocation and climb-controlled dislocation. In order to combine these two regimes and describe them with one unified creep form, a reasonable empirical description on this transition was adopted from [22, 23]. The resulting Zener-Hollomon parameter has a new form as follows:

$$Z_p = A[sinh(\alpha\frac{\sigma}{E})]^n \tag{2.5}$$

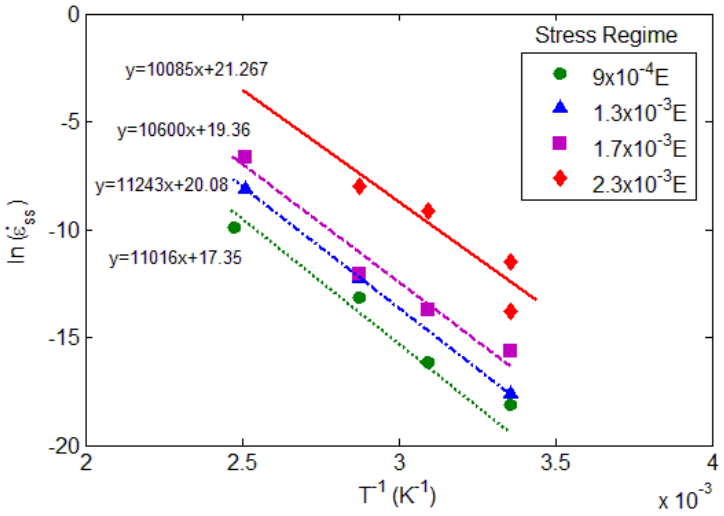

Figure 2.8. Steady strain rate vs. inverse of temperature for unaged cases. Activation energy, Q is determined from slope. Q has a value of 88.85 KJ/mol [15].

where α is the normalized stress coefficient mentioned in Section 2.2.2, which determines at what stress level the power-law (Equation (2.1)) breaks down. This form is more general because it can capture both regimes of Z_p. With the unified creep model described by Equation (2.1), (2.4) and (2.5), next Chavali et al. [15] determined the parameters of this model from creep data under different aging conditions.

Starting with the unaged cases, the normalized stress coefficient, α could be calculated from Figure 2.7. Then, Q, the activation energy could be determined from the slope by plotting $\ln(\dot{\epsilon_{ss}})$ $vs.$ $1/T$ as shown in Figure 2.8:

$$\ln(\dot{\epsilon_{ss}}) = \ln(A) + n\ln(\frac{\sigma}{E}) - \frac{Q}{RT} \tag{2.6}$$

Similarly, the activation energy of other aged conditions could be determined using the same method. The Q values fall within $78 - 88$ KJ/mol range. In the present thesis, Q is assumed to be 88.85 KJ/mol for all cases. The stress exponent, n, is determined from the slope by plotting $\ln(Z_p)$ vs. $\ln(\frac{\sigma}{E})$ as shown in Figure 2.9:

$$\ln(Z_p) = \ln(A) + n\ln(\alpha) + n\ln(\frac{\sigma}{E}) \tag{2.7}$$

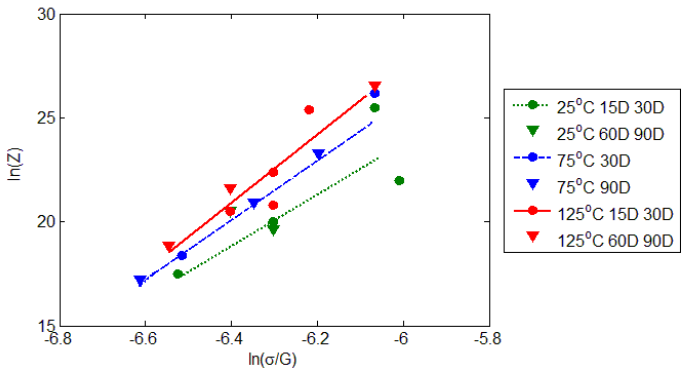

Figure 2.9. Temperature compensated strain rate Z_p vs. $ln(\frac{\sigma}{E})$ at low stress regime [15].

By fitting the experimental data of low stress regime from unaged samples, A is obtained and has a value of $1.53 \times 10^{-8}\ s^{-1}$. Finally, the normalized stress coefficients for aged conditions need to be determined by taking the ratio of Z_p from aged conditions over $Z_{p,0}$ from unaged condition as follows:

$$\frac{Z_p}{Z_{p,0}} = |\frac{[sinh(\alpha\frac{\sigma}{E})]^n}{[sinh(\alpha_0\frac{\sigma}{E})]^{n_0}}|_{\frac{\sigma}{E}=const.} \tag{2.8}$$

The creep experiments were carefully designed so that at different test temperatures, we have the same normalized applied stress $\frac{\sigma}{E}$. In the above equation, α under each aging condition is the only unknown needs to be determined. All evaluations of model parameters in this exponential time-primary-cum-secondary creep model are completed and incorporating microstructural parameters is reviewed below.

2.3.2 Relationship Between Microstructural Parameters and the Unified Creep Model Parameters

As discussed in Section 2.1, $\bar{d}$, the average size of Ag_3Sn precipitates and $\bar{\eta}$, the average size of primary-Sn dendrites, capture the major microstructural evolution due to aging and affect the climb and glide processes of dislocation respectively. Therefore, $\bar{d}$ and $\bar{\eta}$ influence creep behavior of SnAgCu alloys. Extending this reasoning, Chavali

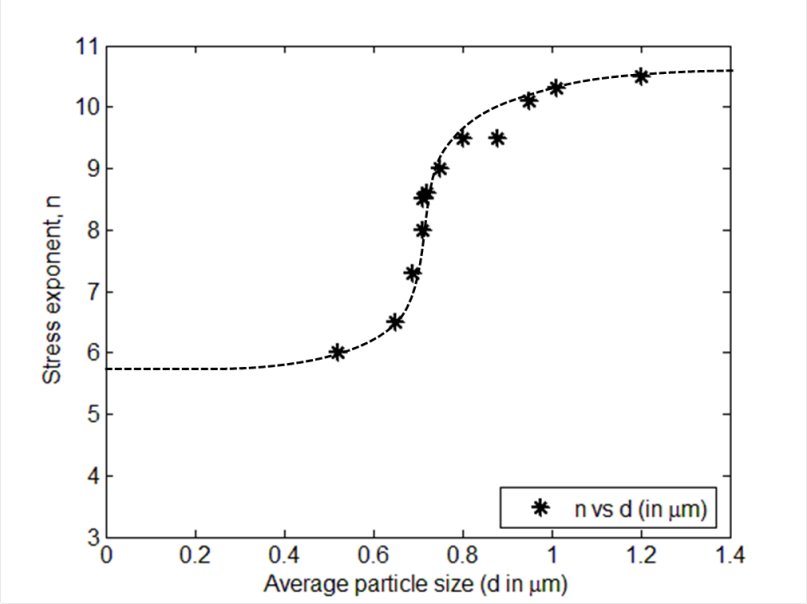

Figure 2.10. Stress exponent vs. average Ag_3Sn particles size [15].

et al. [15] incorporated these two microstructural parameters into the creep model by developing the relationship between stress exponent and the average size of Ag_3Sn precipitates, and the relationship between the normalized threshold stress and the average size of primary-Sn dendrites. The empirical fits based on experiments are shown in Figure 2.10 and Figure 2.11. The fitting functions are below:

$$n = 5.838 + \frac{4.3}{1 + e^{-26.3(\bar{d} - 0.405)}} \tag{2.9}$$

$$\frac{1}{\alpha} = -0.00005\bar{\eta} + 0.002 \tag{2.10}$$

With Equation (2.9) and (2.10), the microstructural parameters influence the parameters of exponential time-primary-cum-secondary creep model. At this point, the microstructurally adaptive creep model is developed fully.

2.4 Summary of Microstructurally Adaptive Creep Model

Compared with the typical models for heterogeneous materials, the microstructurally adaptive creep model developed by Chavali et al. [15] captures the connection

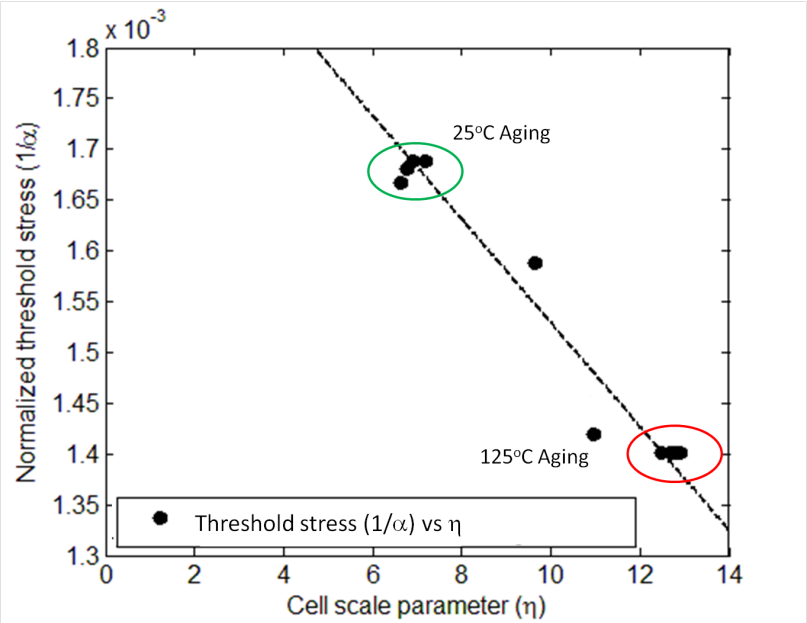

Figure 2.11. Normalized threshold stress vs. average primary-Sn cell size [15].

between microstructural states and mechanical behavior of SnAgCu alloys, which means the effect of aging on mechanical behavior is considered in the model. Starting with the observation on microstructural evolution of Sn3.0Ag0.5Cu samples due to aging, two microstructural parameters, the average size of Ag_3Sn particles, $\bar{d}$, and the average size of primary-Sn dendrites, $\bar{\eta}$, were identified and they affect the glide and climb processes of dislocation. Then an exponential time-primary-cum-secondary creep model was built based on forty-eight creep tests. By expressing two model parameters, the stress exponent and the normalized threshold stress as a function of $\bar{d}$ and $\bar{\eta}$ respectively, the microstructurally adaptive creep model was completed.

3. THE MAXIMUM ENTROPY FRACTURE MODEL

3.1 Typical Fatigue Fracture Models for Solder Alloys

Traditionally, Coffin-Manson rule, Paris Law and models developed from continuum damage mechanics are three major types of fatigue fracture models used for solder alloys [14]. Coffin-Manson rule relates plastic strain to the number of cycles to failure as follows [24, 25]:

$$\frac{\Delta\epsilon_p}{2} = \epsilon_f(2N_f)^c \tag{3.1}$$

where ϵ_p is plastic strain per cycle, N_f is number of cycles to failure and ϵ_f and c are experimental fitting constants. Even though Coffin-Manson rule is popular in industry, it makes an assumption that in each cycle, same extent of plastic strain happens, which is not necessarily true. Since solder joints are small, size of the sample significantly influences the microstructure. However, when data is obtained by testing real solder joints, the obtained parameters depend on the geometry of testing samples. Thus, tests need to be conducted for each package type.

The Paris Law connects the range of stress intensity factor to crack growth [26].

$$\frac{da}{dN} = C\Delta K^m \tag{3.2}$$

where a is crack length, N is the number of cycles, ΔK is the range of stress intensity factor during test, and C and m are empirical fitting constants. Because Paris Law is assumes elastic stresses to drive the crack, it is not suitable for the case where plastic deformation is not negligible as in the case of solder joints.

As for the models based on continuum damage mechanics, material degradation is considered as a state variable connected to load drop versus cycle number [27]. Since damage is an accumulated effect of microcracks, the crack path is difficult to predict.

Overall, the three commonly used fracture models are arguably incomplete. Ideally, fracture models should be geometry-independent, non-empirical, explain the

failure mechanism, applicable to both elastic and plastic cases, and predict crack propagation [14].

3.2 The Maximum Entropy Fracture Model

The Maximum Entropy Fracture Model (MEFM) was developed by Bhate et al. [12]. It was inspired by two experimental observations: (1) the process of crack propagation is thermodynamically irreversible and dissipative, and (2) fracture intrinsically has lengthscale, timescale and/or spatial hierarchy, which is affected by microstructural states. From the second observation, cracks observed at high level of hierarchy, which appear to be deterministic, is the result of uncertain events at lower level of hierarchy related to microstructural variation. By using Information Theory [28] along with maximum entropy principle of statistical mechanics, a form of damage was derived which minimizes the influence of the uncertainty of microstructural states on the fracture at higher levels of hierarchy. The irrecoverable energy from new surface creation or plastic dissipation was connected to the damage in microstructural states with continuum thermodynamics and J2 plasticity theory. Finally, Bhate et al. [12] demonstrated the model using experimental data from SnPb solder joints. Chan et al. [13] demonstrated the MEFM by extracting the damage accumulation parameters for Sn3.8Ag0.7Cu solder joints with isothermal cyclic fatigue tests. Later the model was validated by applying the damage accumulation parameter in FEA model to predict crack initiation and propagation in Sn3.8Ag0.7Cu solder joints of a wafer-level chip-scale package (WLCSP). The FEA model accurately captured the shape of crack front and predicted the number of cycles which corresponds to the experimental crack profile within 10% error. Details of the Maximum Entropy Fracture Model could be reviewed in [12, 13]. Some essential concepts are covered in the following sections.

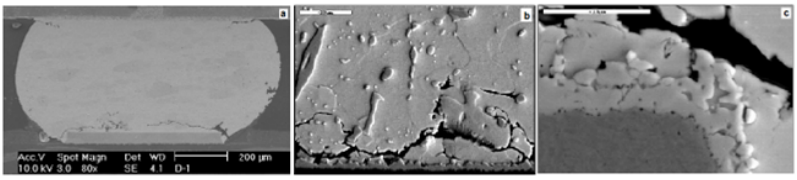

Figure 3.1. (a) Cracks in a solder joint. (b) Higher magnification shows development of cracks and presence of intermetallic compounds. (c) Higher magnification reveals crack propagates through the bulk solder, but not the intermetallic [12].

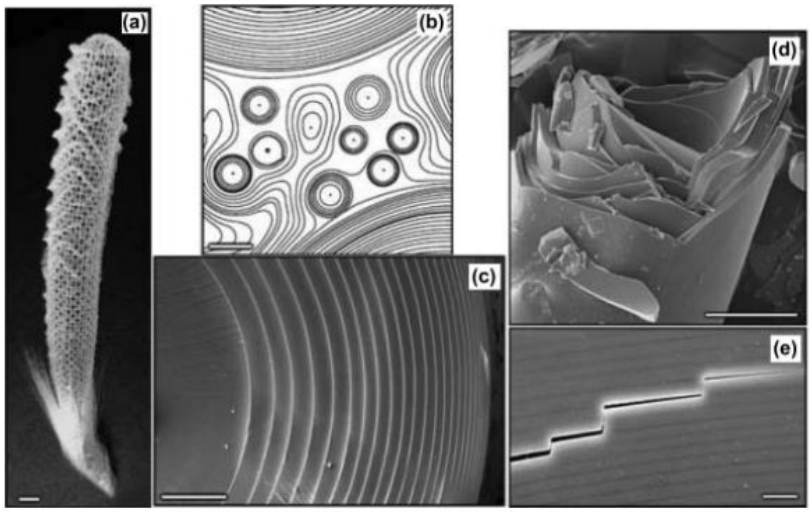

Figure 3.2. Hierarchy in the structure of sea sponge, Euplectella [29].

3.2.1 Hierarchical Fracture Process and Information Theory

The influence of hierarchical structural lengthscale on crack growth exists commonly in both engineering and nature. An engineering example of hierarchical fracture is shown in Figure 3.1. At lower hierarchy, the microstructure shows greater variation. Variation in the grain size or orientation could result in different local fracture propagation direction at lower lengthscale. However, the crack path at higher lengthscale is predictable and is largely dictated by geometry and loading.

A perfect example of structural hierarchy in nature is Euplectella, the sea sponge in Figure 3.2. There are three levels of structural hierarchy in the failure of Euplectella.

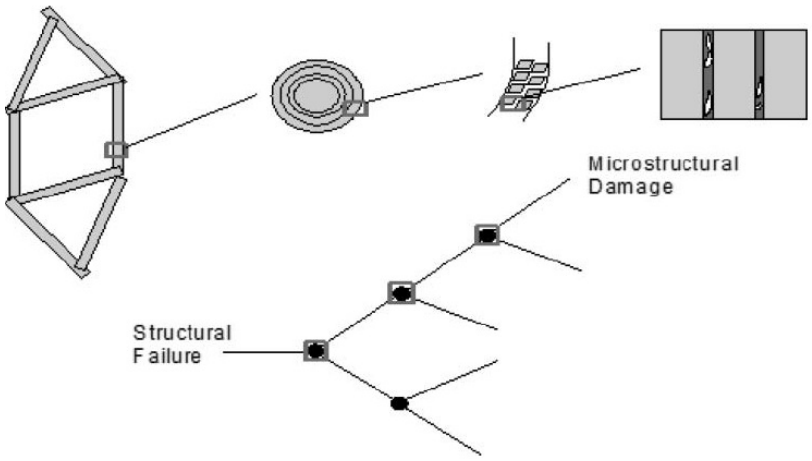

Figure 3.3. Decision tree describing the hierarchy in fracture [12].

In order to fracture the strut (a) in Euplectella, cracks are required to propagate through silica matrix (b) and spicule (d), which needs a fracture of the glass layers (c) and organic layers (e) at lower lengthscale.

Because fracture process is intrinsically hierarchical, it could be well described by a decision tree in Figure 3.3. The leaves of tree represent lower hierarchy, the microstructural states, and the nodes represent appropriate lengthscale or time events. Because of this inherent hierarchy, the structural failure may occur through different microstructural failure possibilities.

The uncertainties due to the hierarchical nature of fracture is described using Information Theory in the Maximum Entropy Fracture Model. When developing the Information Theory, Shannon [28] put forward the information entropy H, an abstract measure of uncertainty associated with event x_i as follows:

$$H = -k \sum_{i}^{n} p_i \ln(p_i) \tag{3.3}$$

where n is the number of possible events and p_i is the probability of an event occurring. Shannon argued that the information entropy H should have these following properties:

1. Continuity. H should be a continuous function of p_i.

2. Monotonicity. If all p_i are equal and $p_i = \frac{1}{n}$, then H should continuously increase with n, which means that if more equally likely events are possible, the uncertainty increases.

3. Composition. If an event be broken down into two successive events, the original H should become the weighted sum of those two individual values of H with appropriate conditional probability based on the events at lower hierarchical structure.

Starting from these three postulates of continuity, monotonicity, and composition, Shannon proved that the only mathematical form of information entropy satisfying these three assumptions is:

$$H = -k \sum_{i}^{n} p_i \ln(p_i) \tag{3.4}$$

where k is a positive constant.

The information entropy has no specific physical meaning, however, it could be connected to the Boltzmann H-function defined as [30]:

$$H = \sum_{i}^{n} p_i \ln(p_i) \tag{3.5}$$

and to the Gibbs entropy formula as:

$$s = -k_B \sum_{i}^{n} p_i \ln(p_i) \tag{3.6}$$

where s is the entropy and k_B is Boltzmann constant. When the probabilities are equal, the Gibbs expression reduces to the Boltzmann H function. Based on above, the information entropy, the measure of information uncertainty developed by Shannon, generalizes the concept of thermodynamical entropy of physical system.

3.2.2 Maximum Entropy Principle and the Probability of a Microstructural State

As shown in Figure 3.3, the microstructural states could be represented by the leaves in the decision tree with p_i being the probability of the case obtained by

going from leaf to root. Let $p_{j/i}$ be defined as the probability going from j^{th} level in hierarchical structure to event x_i, then we have:

$$p_i = \prod^{j} p_{j/i} \tag{3.7}$$

and also:

$$\sum_{i}^{n} p_i = 1 \tag{3.8}$$

Suppose the probability of fracture at a point of interest depends on the energy measure $\psi(x)$ at that point. Based on the uncertainty in the microstructural states mentioned earlier, the expected energy measure associated with the microstructural states is:

$$\langle \psi(x) \rangle = \sum_{i}^{n} p_i \psi_i \tag{3.9}$$

where $\psi_i = \psi(x_i)$. Based on Jaynes' work [30], Bhate et al. [12] argued that by maximizing the information entropy, the relationship between energy measure ψ and the probability p_i could be determined. The expression relating probability of event x_i to the energy measure ψ_i is as follows:

$$p_i = exp(\frac{-\mu\psi_i - \lambda - k}{k}) \tag{3.10}$$

where μ and λ are Lagrange multipliers obtained by satisfying Equation (3.7) and (3.8). The probability of microstructural state is a monotonic function of ψ_i.

3.2.3 Energy Measure of Damage

Considering for now only two states existing in microstructure, namely, intact state or failed state, with x_0 being the intact state and x_1 the failed state. From Equation (3.10), we have:

$$p_0 = exp(-\frac{0 - \langle \psi(x) \rangle}{k_\psi} - c_\psi) \tag{3.11}$$

$$p_1 = exp(-\frac{\psi_1 - \langle \psi(x) \rangle}{k_\psi} - c_\psi) = p_0 exp(-\frac{\psi_1}{k_\psi}) \tag{3.12}$$

Now let's extend to the case when n microstructural states exist between intact and failure and p_i is the probability corresponding to each state. Each state has different energy measure ψ_i because of monotonic relationship between ψ_i and p_i mentioned before. Assume ψ is a monotonic and continuous time-dependent function with $t \in [0, \infty]$, which allows material degradation with time. The above discrete description can be made a continuous distribution function using probability density function in statistical mechanics [31] as follows:

$$p(t_i \leq t \leq t_i + dt) = p_0 exp(-\frac{\psi(t_i)}{k_\psi}) \equiv f(t_i)dt \tag{3.13}$$

where $f(t)$ is the probability density function. If material behavior doesn't rely on time, t describes material degradation as a "pseudo" time parameter. Then, the corresponding cumulative distribution function $D(t)$ is:

$$D(t) = \int_0^t f(\tau)d\tau = \int_0^t f(0)exp(-\frac{\psi(\tau)}{k_\psi})d\tau \tag{3.14}$$

Since $D(t)$ increases continuously from 0 to 1 as t increases, $D(t)$ could be used to measure accumulated damage.

When failure occurs, the material loses its ability to bear load because of crack propagation. This is an irreversible process with energy loss when new surfaces are created. Bhate et al. [12] derived a relationship between entropic dissipation and inelastic dissipation with equilibrium thermodynamics and $J2$ plasticity theory.

$$\dot{\psi} \equiv \frac{1}{\rho T}[\sigma_0^Y \dot{\epsilon_1} + \sigma_1^* \dot{\epsilon_1} + \sigma_{ij}^* \dot{\epsilon_{ij}^*}] \tag{3.15}$$

where ρ is the density of the material, T is absolute temperature, σ_0^Y is the yield stress, σ_1^* is the yield surface radius, σ_{ij}^* is the back stress, $\dot{\epsilon_1}$ is the equivalent plastic strain rate and $\dot{\epsilon_{ij}^*}$ is the rate of plastic strain conjugate to the back stress. The material is assumed to be an isotropic, elastic-perfectly plastic material governed by $J2$ plasticity subject to kinematic hardening. Combining Equation (3.14) and (3.15), we have:

$$D(t_0) = \int_0^{t_0} f(0)exp(-\int_0^{t_0} \frac{1}{\rho k_\psi T}[\sigma_0^Y \dot{\epsilon_1} + \sigma_1^* \dot{\epsilon_1} + \sigma_{ij}^* \dot{\epsilon_{ij}^*}]dt)d\tau \tag{3.16}$$

$$= \int_0^{t_0} f(0) exp(-\int_0^{t_0} \frac{\dot{W}_t}{\rho k_\psi T} dt) d\tau \tag{3.17}$$

where $\dot{W}_t$ is the rate of inelastic dissipation. Further, assuming the inelastic dissipation rate is constant, since $D(\infty) = 1$, Equation (3.17) can be simplified to:

$$D = 1 - exp(-\frac{W_t}{\rho k_\psi T}) \tag{3.18}$$

where k_ψ is the damage accumulation parameter. Equation (3.18) relates accumulated damage, D, to total accumulated inelastic dissipation, W_t.

3.3 Isothermal Cycling Tests and Damage Accumulation Parameter Extraction

The equipment, experimental setup and procedure, and method to calculate the damage accumulation parameter for Sn3.8Ag0.7Cu solder alloy will be reviewed below and more details could be found in [13]. In this study, similar experiment and extraction method are adopted for Sn3.0Ag0.5Cu solder alloy, which will be covered in Chapter 4.

3.3.1 Equipment, Experimental Setup and Test Samples

The isothermal cyclic loading tests on Sn3.8Ag0.7Cu samples at different temperature were conducted by a custom-built microscale mechanical tester as shown in photograph in Figure 3.4 and schematic in Figure 3.5. This microscale mechanical tester has high resolution to achieve sub-micron displacement by a precision linear stage (Newmark 250076-SM). It also contains a six-axis load cell (JR3 90M31A-I50) to gather the data of shear load applied on test samples. In order to accurately align those two lap bars, two accurate manual stages (Newport UMR8.51) are installed between bracket and the load cell. A capacitance sensor with sub-micron resolution and a sensor target (an aluminum block with polished surface) are mounted on the lap bars to form a closed-loop measurement system, which avoids compliance in load

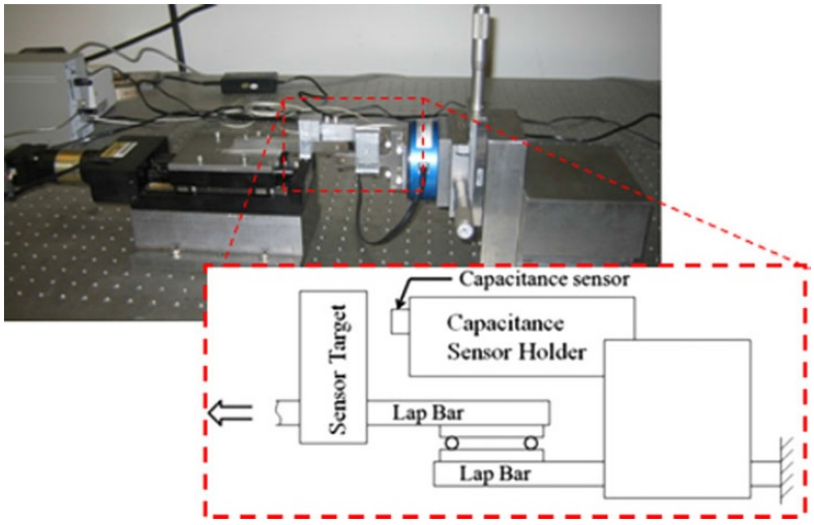

Figure 3.4. Photograph of microscale mechanical tester and the schematic showing the mounting of the capacitance sensor [13].

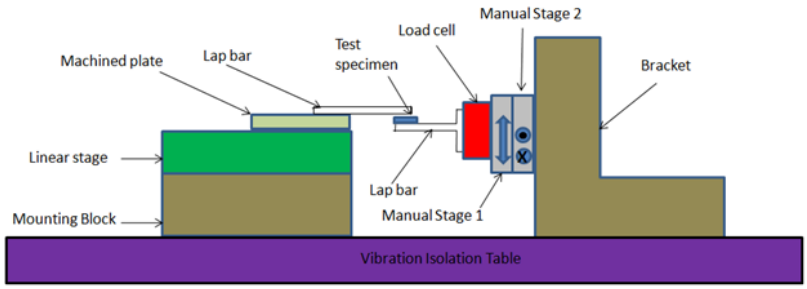

Figure 3.5. Schematic of microscale mechanical tester [14].

train and ensures the accuracy of constant strain rate control [18,32]. The whole test system is controlled via a software interface built in Labview2009, which could control the linear stage to perform creep test, monotonic movement, and cyclic loading. More details are covered in [13].

Figure 3.6 shows the design of samples. The solder joints at the four corners of the assembly have a specific aspect ratio ($Aspect\ Ratio = \frac{standoff\ height}{pad\ diameter} = \frac{240\mu m}{650\mu m}$). This is because the samples with low aspect ratio minimize the degree of stress heterogeneity at the pad interface, ensuring a state of pure shear. This aspect ratio was validated by using ABAQUS Implicit Dynamics FE software and compared with other aspect

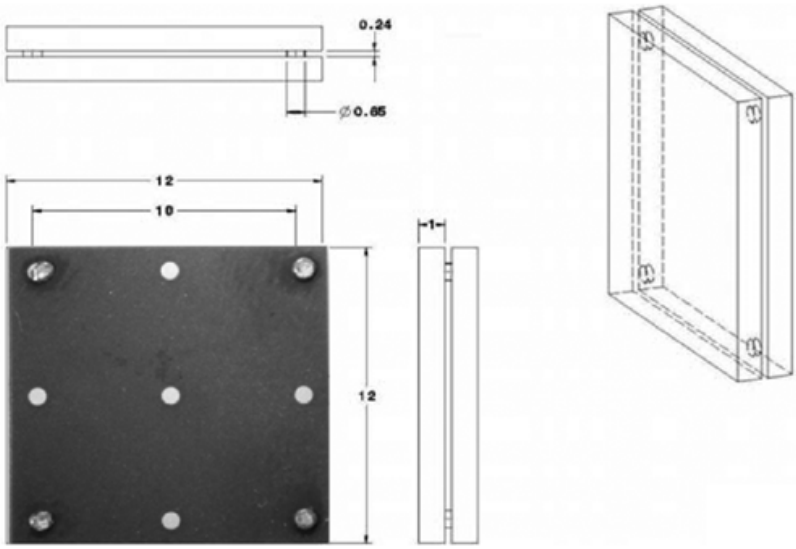

(a)

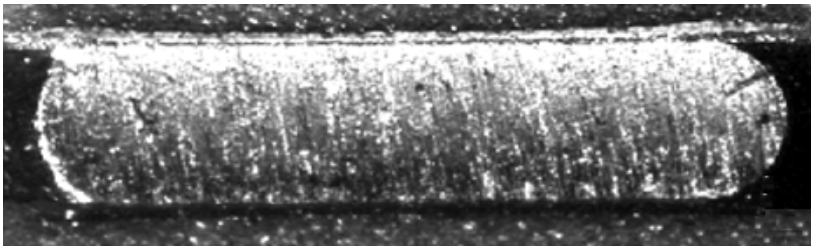

(b)

Figure 3.6. (a) Schematic of sample showing dimensions and solder joints sandwiched at four corners. (b) Image from SEM showing cross section of solder joint [18].

ratios by Bhate et al in [18]. The samples were stored in a refregirator at $-10°$C prior to testing to minimize isothermal aging effect.

3.3.2 Experimental Procedure

The samples were bonded to the lap bars as shown in Figure 3.5. For 25°C tests, a cyanoacrylate adhesive was used for bonding. While at 125°C tests, a two-part epoxy adhesive from MasterBond (Part# EP-31) was applied instead. Once the test begins, the linear stage moves driven by a motor and the lap bar attached to the linear stage

Table 3.1. Cyclic fatigue tests at different temperature and different shear strain rates [1].

		Applied Strain Rate during Loading	
		$6.94 \times 10^{-5} s^{-1}$	$6.94 \times 10^{-4} s^{-1}$
Test Temp	25C	√	√
	75C		√
	125C	√	

moves as well, applying shear force on sample. The strain control profile is shown in Figure 3.7. Over the cycle, the profile imposes up to 5% of equivalent strain, followed by a hold for 100 s, ramp down to 0% over the same duration as ramp up and hold for 100 s again before starting the next cycle. The test matrix is shown in Table 3.1. From cyclic loading tests, load vs. displacement profile and stress drop vs. number of cycles data could be obtained as shown in Figure 3.8.

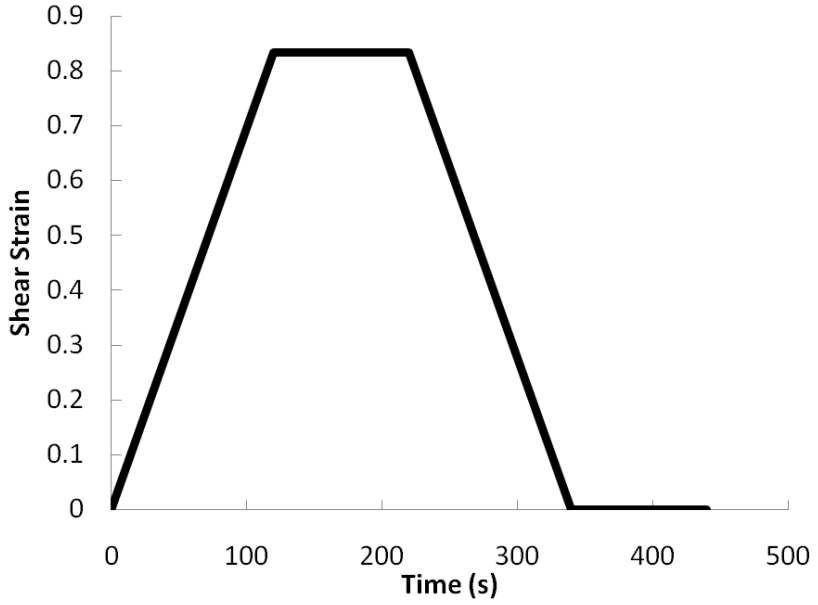

Figure 3.7. Strain control profile with shear strain rate $6.94 \times 10^{-4}\ s^{-1}$ [1].

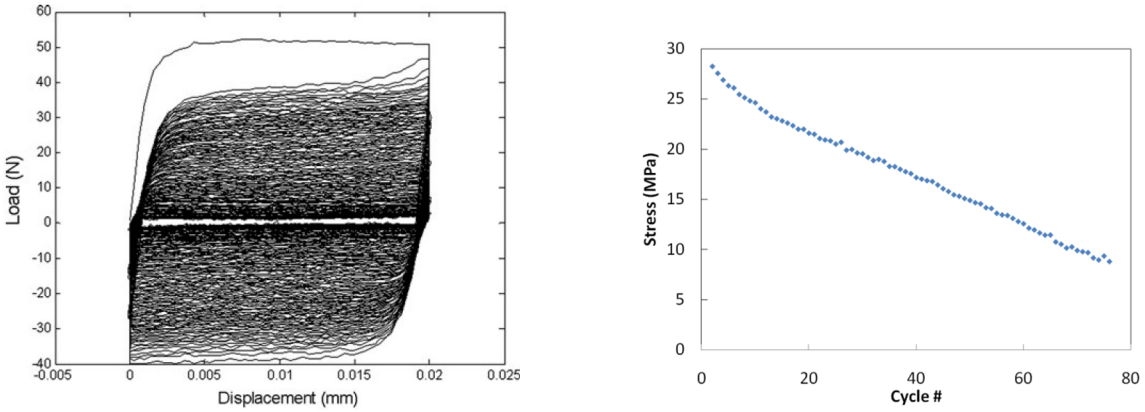

Figure 3.8. Load vs. displacement, stress drop vs. number of cycles from Sn3.8Ag0.7Cu fatigue test at 25°C with shear strain rate of $6.94 \times 10^{-4}\ s^{-1}$ [13].

3.3.3 Extraction of the Damage Accumulation Parameter

The damage accumulation parameter is extracted from Equation (3.18) by a data fit to cyclic fatigue data beginning with Equation (3.18):

$$D = 1 - exp(-\frac{W_t}{\rho k_\psi T})$$

where W_t is the total accumulated inelastic dissipation as shown in Figure 3.9 and it consists of two parts: plastic dissipation and creep dissipation. Plastic dissipation can be calculated by summing the area under strain-stress curve of each cycle from experimental data. The time-hardening creep model was used to calculate creep dissipation by Chan et al [13]:

$$\epsilon_{cr} = K\sigma^n t^q e^{-Q_1/RT} + B\sigma^m t e^{-Q2/RT} \tag{3.19}$$

where ϵ_{cr} is the total creep strain, σ is the constant applied stress, t is time in seconds, T is absolute temperature, others are material constants.

Since damage is a description of material degradation, the loss of ability to bear load could be considered as damage. Hence, the stress drop data from cyclic fatigue is a good estimation for damage and defined as follows [13]:

$$D = (1 - \frac{\bar{\sigma_i}}{\bar{\sigma_{max}}}) \tag{3.20}$$

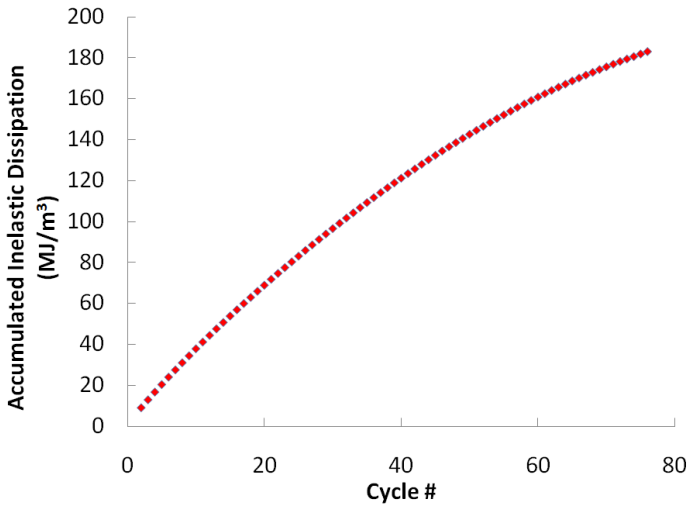

Figure 3.9. Total accumulated inelastic dissipation vs. number of cycles at 25°C [13].

where $\bar{\sigma}_i$ is the average peak stress of tensile (1^{st} half of loading cycle) and compression (2^{nd} half of loading cycle) in each cycle and $\bar{\sigma_{max}}$ is the maximum average peak stress among all cycles. Typically the $\bar{\sigma}_i$ in the second cycle will be considered as $\bar{\sigma_{max}}$, because in the first cycle, the sample is subject to tensile stress from 0 initial strain, while in other cycles, tensile loading starts from a compressive strain state.

By equating Equation (3.20) and (3.18), the damage accumulation parameter k_ψ could be extracted from cyclic fatigue data by a fit on a semilog scale. As a demonstration, k_ψ is extracted for Sn3.8Ag0.7Cu samples at 25°C with shear strain rate of $6.94 \times 10^{-5}\ s^{-1}$ from Figure 3.10. All k_ψ values of the tests in test matrix are close to each other with only 3% variation. Thus, these tests substantiate that k_ψ is independent of temperature and strain rate [1].

3.4 Numerical Prediction Validated against Experimental Results

With the single damage accumulation parameter extracted above, a finite-element model of a wafer-level chip-scale package (WLCSP) with Sn3.8Ag0.7Cu solder joints was built in ABAQUS as shown in Figure 3.11 [13]. Figure 3.12 shows that this model

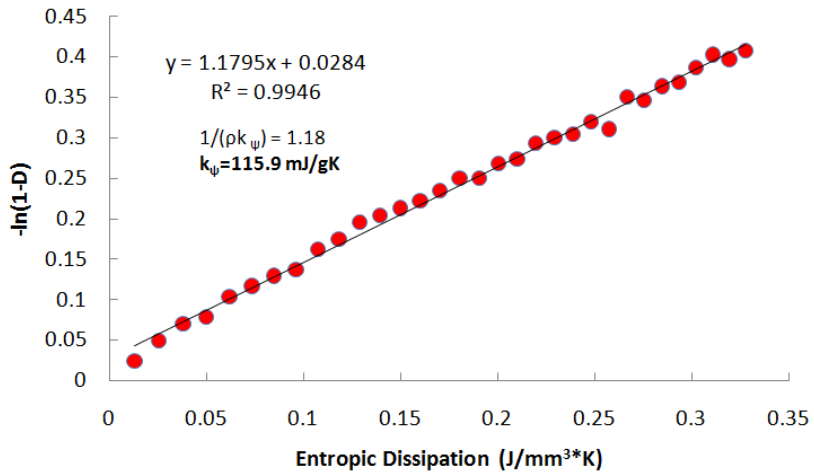

Figure 3.10. The damage accumulation fit for Sn3.8Ag0.7Cu solder joint at 25°C with shear strain rate of $6.94 \times 10^{-5}\ s^{-1}$ [1].

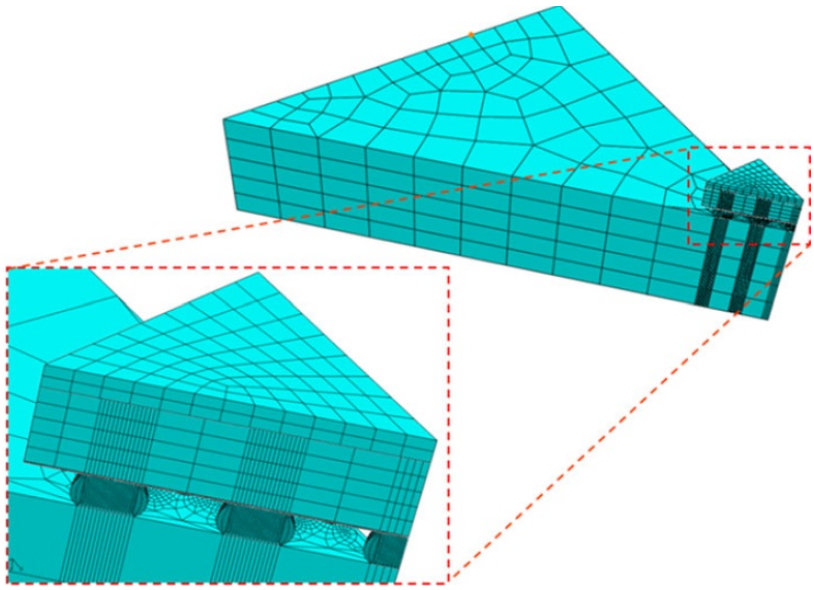

Figure 3.11. FE model built in ABAQUS with symmetric boundary conditions, including two complete solder joints, four half joints, and one one-eighth joint [13].

could capture the profile of crack front accurately and predict the number of cycles corresponding to the observed crack front profile within 10% of the measured number of cycles from experiment.

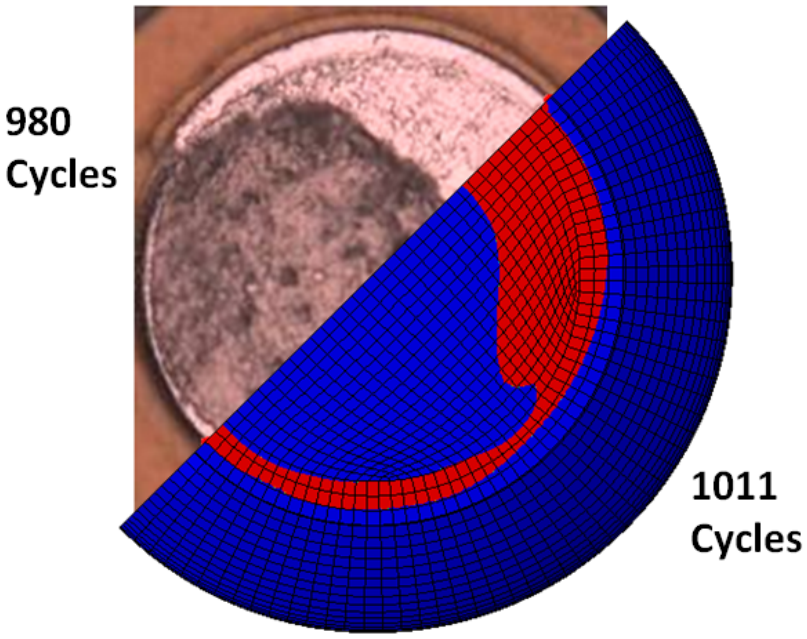

Figure 3.12. Comparison of crack front profile from numerical prediction against experimental measurement [13].

3.5 Summary of The Maximum Entropy Fracture Model

In present chapter, three types of traditional fatigue fracture models, namely, Coffin-Manson rule, Paris Law and models based on continuum damage mechanics, were reviewed and compared. The Maximum Entropy Fracture Model was proposed as a geometry-independent, non-empirical fracture model by Bhate et al. [12]. The key concepts behind the development of MEFM were reviewed. Next, the experimental method and extraction procedure of damage accumulation parameter for Sn3.8Ag0.7Cu solder alloy are elaborated. Finally, a FE model using damage accumulation parameter was built and the numerical prediction was validated against experimental result. In next chapter, the construction of constitutive models for Sn3.0Ag0.5Cu solder joints will be discussed first and followed by fatigue characterization.

4. FATIGUE CHARACTERIZATION OF SN3.0AG0.5CU SOLDER JOINTS USING MAXIMUM ENTROPY FRACTURE MODEL

4.1 Constitutive Modeling for Different Aging Conditions

In Chapter 2, the microstructurally adaptive creep model proposed by Chavali et al. was reviewed. In order to develop the constitutive models for different aging conditions, the corresponding microstructure needs to be characterized. The pretest aging conditions to which the samples were subject are shown in Table 4.1. The samples were placed inside an oven at 125°C to carryout isothermal aging from 0 to 60 days. Prior to isothermal aging, the samples were stored at −10°C to minimize aging. Once the isothermal aging was completed, the microstructure of the samples were characterized under an SEM as described in Section 2.1. The microstructural evolution under different aging conditions are shown in Figure 4.1 and 4.2.

As aging time becomes longer, Ag_3Sn particles coarsen and disperse, while at the same time the primary-Sn dendrite cells become larger. The characterized microstructural parameters under different aging conditions are summarized in Table 4.2.

Based on Equation (2.9) and (2.10), the stress exponent and the normalized threshold stress coefficient were determined for each aging condition. They are summarized in Table 4.3. With Equation (2.1), (2.4) and (2.5) as shown below, the

Table 4.1. Isothermal aging inside an oven at 125°C from 0 to 60 days.

	Aged at 125C			
Aging Day(s)	Unaged	15 Days	30 Days	60 Days
# of Samples	3	3	3	3

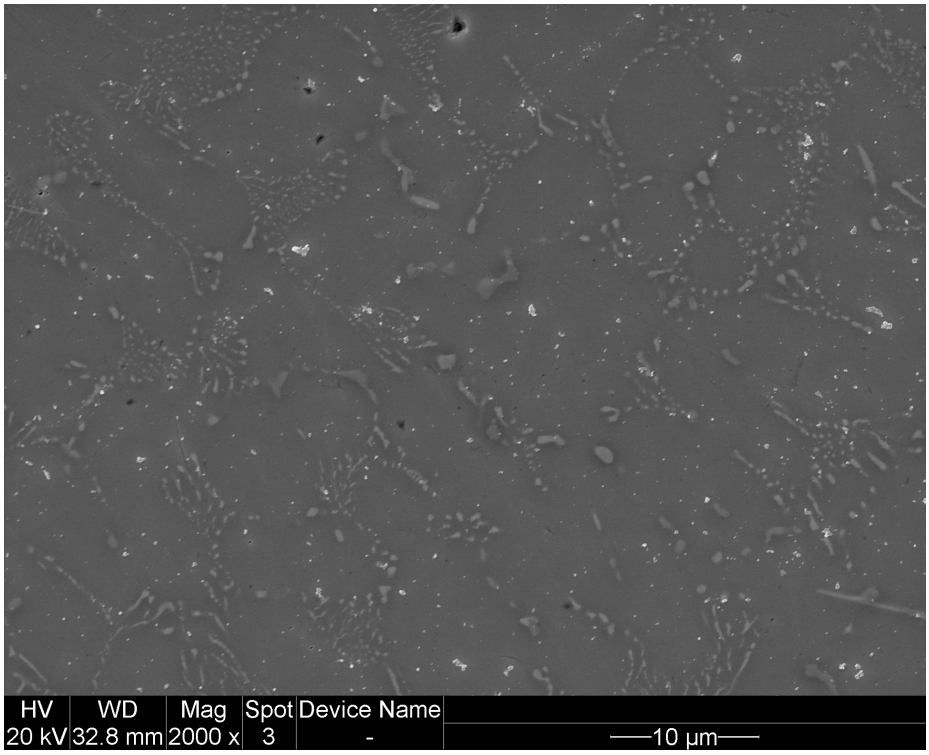

(a)

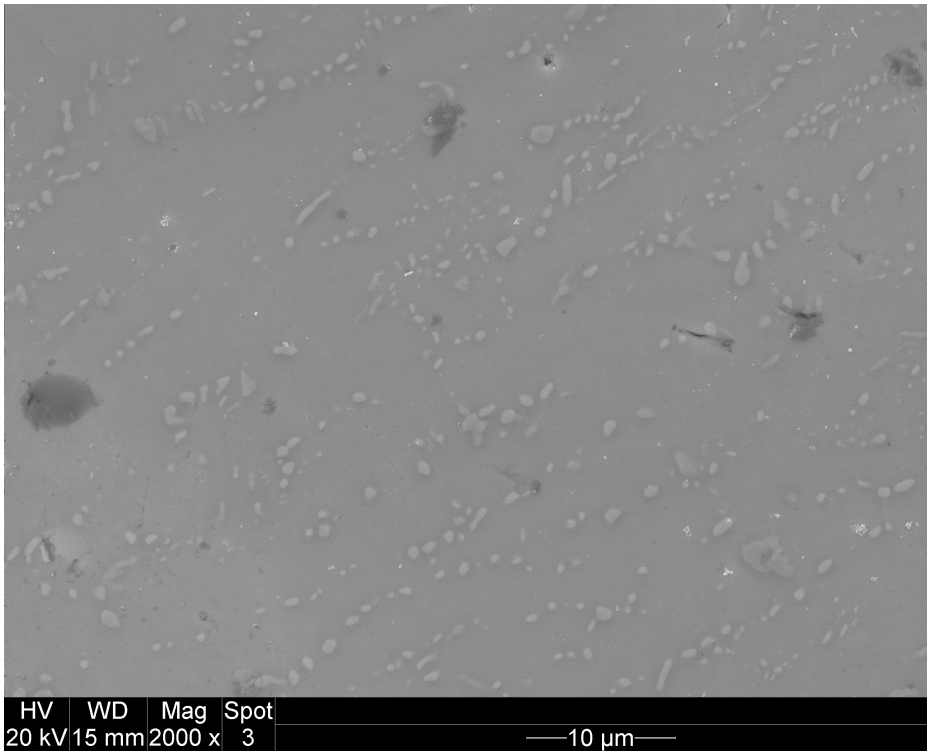

(b)

Figure 4.1. Microstructural evolution: (a) unaged sample and (b) 15-day aged sample at 125°C.

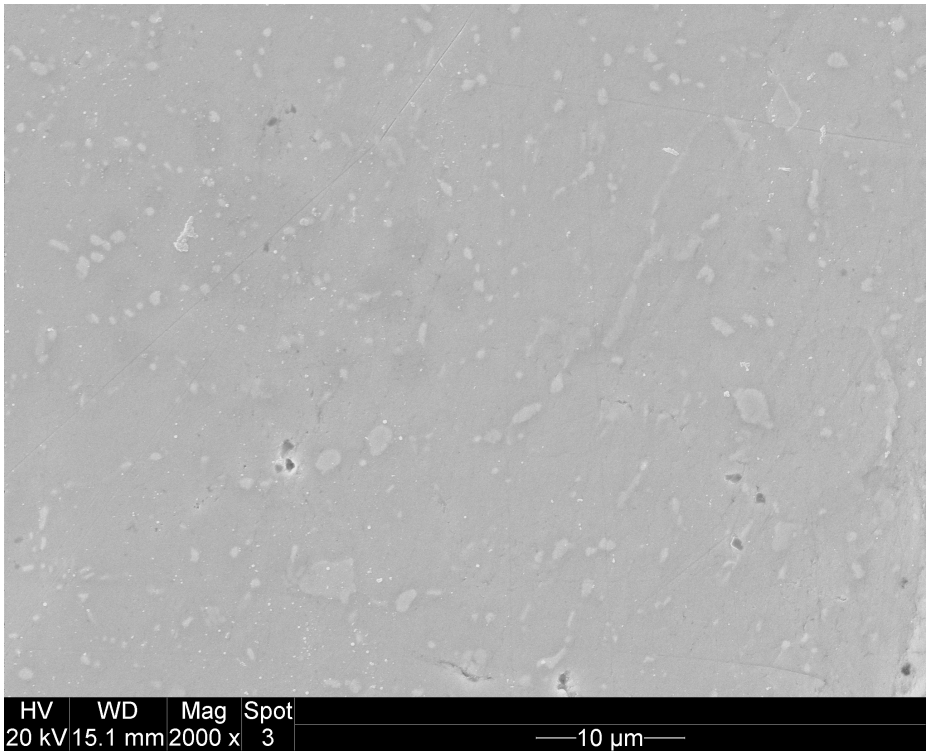

(a)

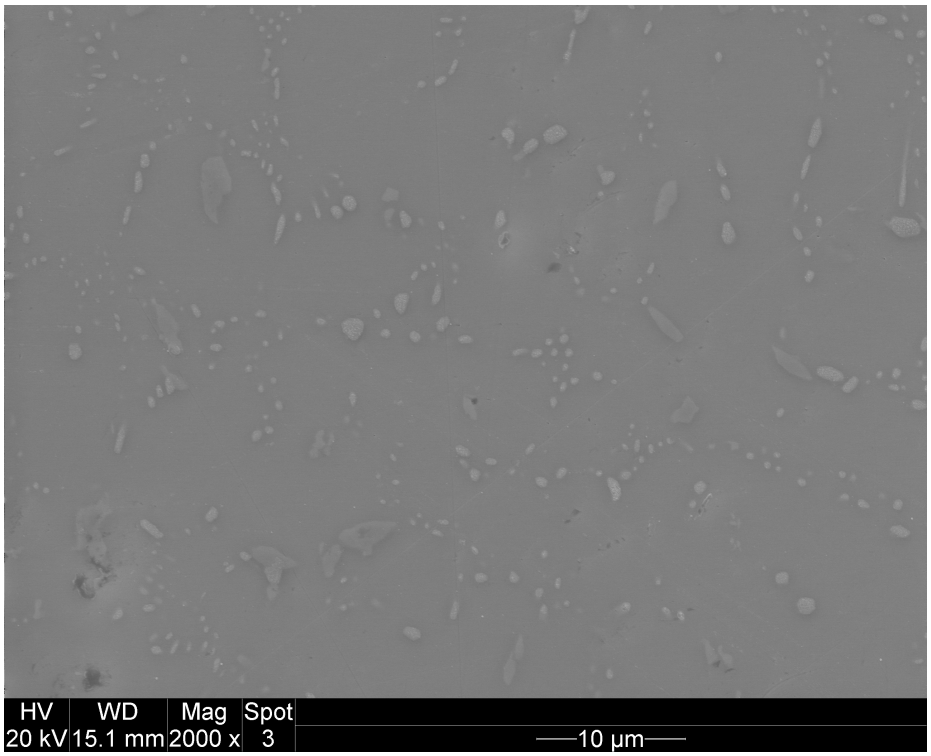

(b)

Figure 4.2. Microstructural evolution: (a) 30-day aged sample and (b) 60-day aged sample at 125°C.

Table 4.2. Average size of Ag_3Sn particles, $\bar{d}$, and average size of primary-Sn dendrites, $\bar{\eta}$ under different aging conditions.

	0D (Unaged)	15D	30D	60D
$\overline{d}$ μm	0.49	0.98	1.10	1.16
$\overline{\eta}$ μm	6.33	11.86	12.29	12.91

Table 4.3. The stress exponent, n, and the normalized threshold stress coefficient, α, for different aging conditions.

	0D (Unaged)	15D	30D	60D
n	5.91	10.14	10.14	10.14
α	594.00	706.71	721.76	727.27

construction of a microstructurally adaptive creep models for different aging conditions is complete at this point.

$$Z_p = A[sinh(\alpha\frac{\sigma}{E})]^n$$

$$Z_p = \dot{\epsilon}_{ss}e^{Q/RT}$$

$$\epsilon = \epsilon_t(1 - e^{-k\dot{\epsilon}_{ss}t}) + \dot{\epsilon}_{ss}t$$

Thus, estimations of the Zener-Hollomon parameter, Z_p, the minimum creep strain rate, $\dot{\epsilon}_{ss}$, and the total creep strain, ϵ, in each test is now possible with the obtained constitutive models. Also, the accumulated creep dissipation, $W_{rate-dependent}$, can be estimated with the constitutive models to extract damage accumulation parameter in MEFM.

4.2 Experimental Setup, Procedure and Test Matrix

The method adopted in this study to extract the damage accumulation parameter for Sn3.0Ag0.5Cu is similar to that used by Chan et al. in Section 3.3.2. The

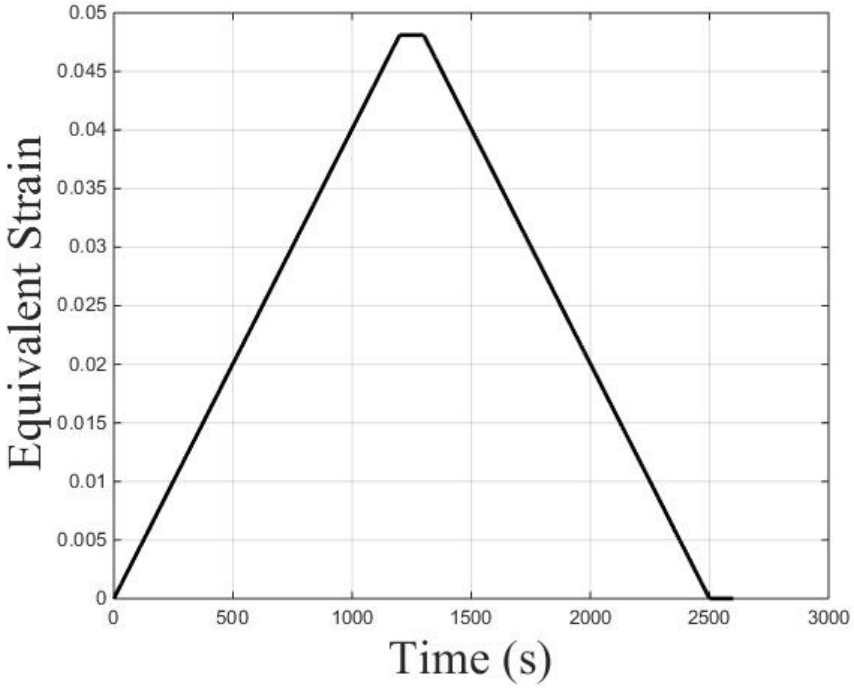

Figure 4.3. Strain control profile of cyclic fatigue test at the strain rate of $4 \times 10^{-5}\ s^{-1}$.

equivalent strain rate in cyclic fatigue test is fixed at $4 \times 10^{-5}\ s^{-1}$ in this study as shown in Figure 4.3. The strain is ramped from 0 to 1200 s, and then held for 100 s. The strain is then ramped down to 0 at the same strain rate and held for 100 s again before next cycle. From cyclic fatigue tests, the load vs. displacement relationship is obtained as shown in Figure 4.4.

The design of test samples used here is identical to that described in Chapter 3, but the solder joint material is Sn3.0Ag0.5Cu instead. These test samples have a specific aspect ratio to ensure a homogeneous stress state at the pad interface. As a result, the following calculation of equivalent stress/strain becomes possible for each load:

$$\sigma = \sqrt{3}\frac{P}{A} \tag{4.1}$$

$$\epsilon = \frac{1}{\sqrt{3}}\frac{\delta}{h} \tag{4.2}$$

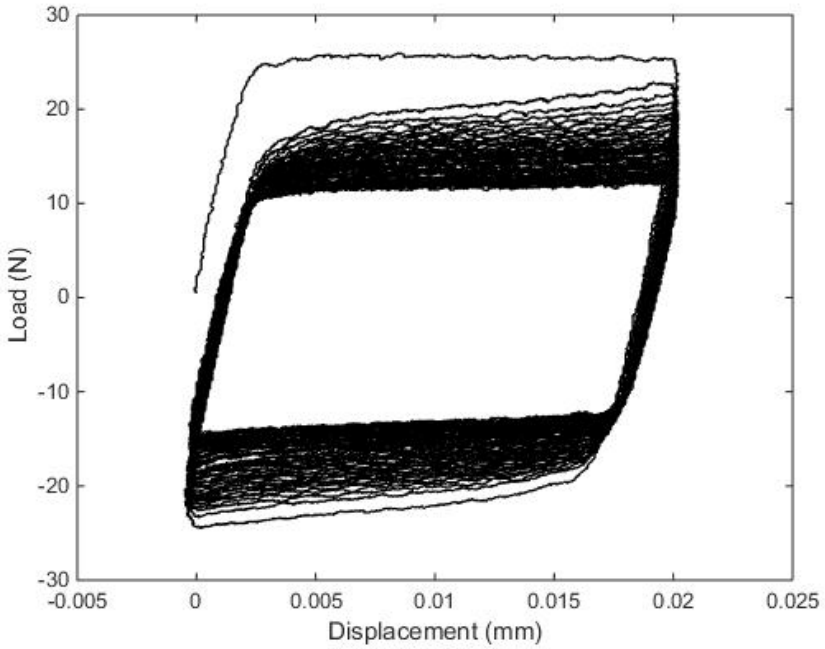

Figure 4.4. Load vs. displacement from 30-day aged Sn3.0Ag0.5Cu sample at 100°C.

where P is the applied shear load on each solder joint, A is the pad area, δ is the shear displacement and h is the standoff height. More details about sample design is discussed in [13].

The test matrix in this study is shown in Table 4.4. Prior to the test, the samples were taken out from a refrigerator and placed inside an oven at 125°C to carryout isothermal aging from 0 to 60 days. For experiments performed at 100°C, a custom-built environmental enclosure was used as shown in Figure 4.5. Hot air was circulated inside the chamber driven by a commercial environmental controller. A k-type thermocouple was used to detect the temperature of air inside the enclosure and was used to control the temperature in closed-loop.

Table 4.4. Test matrix of Sn3.0Ag0.5Cu solder joints.

Aging Days(125C)	25C	100C
0D		
15D		
30D		
60D		

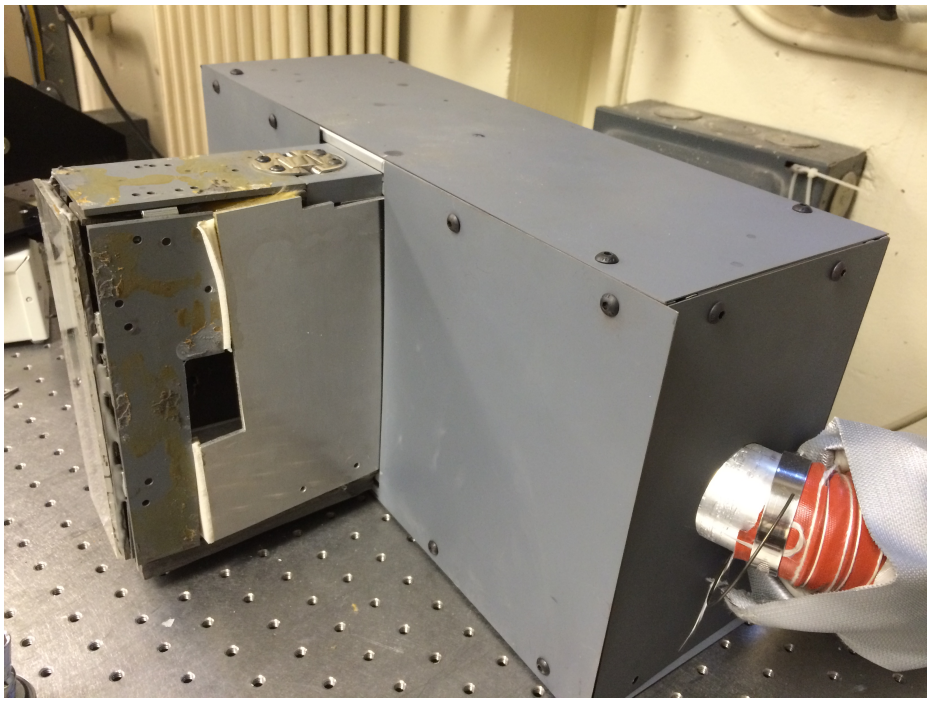

Figure 4.5. A custom-built environmental enclosure covered the sample, capacitance sensor and part of the lap bars during the 100°C fatigue tests.

4.3 Extraction of the Damage Accumulation Parameter

Using the procedure described in Section 3.3.3, the damage accumulation parameter were determined through a linear fit on semilog plot of Equation (3.18):

$$D = 1 - exp(-\frac{W_t}{\rho k_\psi T})$$

W_t, the total accumulated inelastic dissipation was determined by summing up the inelastic dissipation in each cycle as shown in Figure 4.6 and 4.7. The dissipation consists of two parts:

$$W_t = W_{rate-independent} + W_{rate-dependent} \tag{4.3}$$

$W_{rate-independent}$ is plastic dissipation independent of strain rate and it could be calculated by summing the area under stress-strain curve of each cycle from experimental data. And $W_{rate-dependent}$ is the summation of creep dissipation in each cycle. For each aging condition, the corresponding adaptive creep model developed in Section 4.1 was utilized to calculate $W_{rate-dependent}$. Compared with the time-hardening creep model used by Chan et al., adaptive creep model considers the aging effect on creep behavior by incorporating microstructural parameters into creep model.

The damage D is determined from stress drop data as shown in Figure 4.8 based on Equation (3.20) as follows:

$$D = (1 - \frac{\bar{\sigma_i}}{\bar{\sigma_{max}}})$$

where $\bar{\sigma_i}$ is the average of peak stress during tensile (1^{st} half of loading cycle) and compressive (2^{nd} half of loading cycle) portions in each cycle and $\bar{\sigma_{max}}$ is the maximum average peak stress among all cycles.

By equating Equation (3.20) and (3.18), we have:

$$-\ln(1 - D) = \frac{1}{\rho k_\psi} S \tag{4.4}$$

$$S = \frac{W_t}{T} \tag{4.5}$$

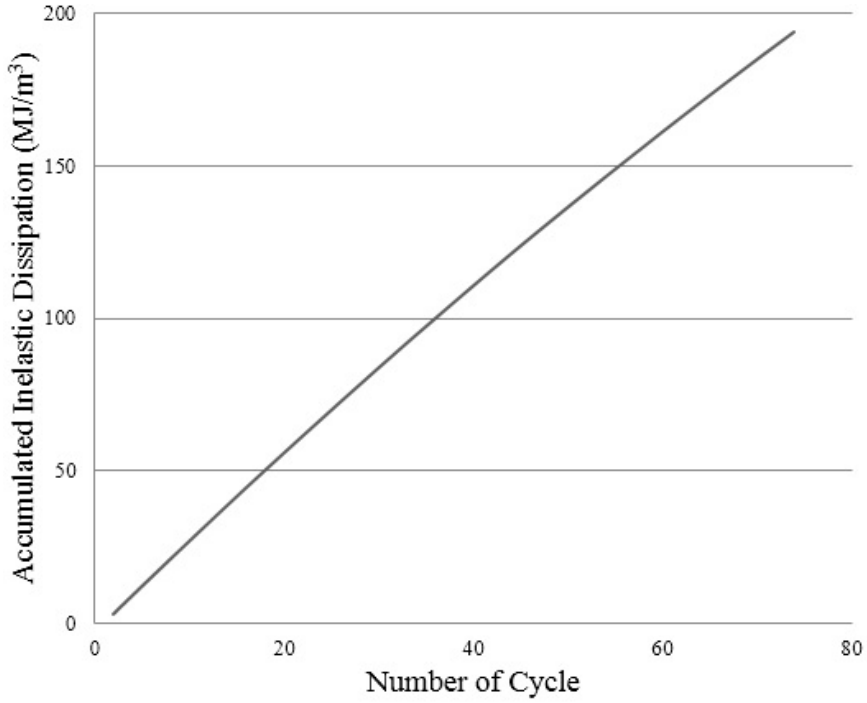

(a) Unaged sample at 25°C

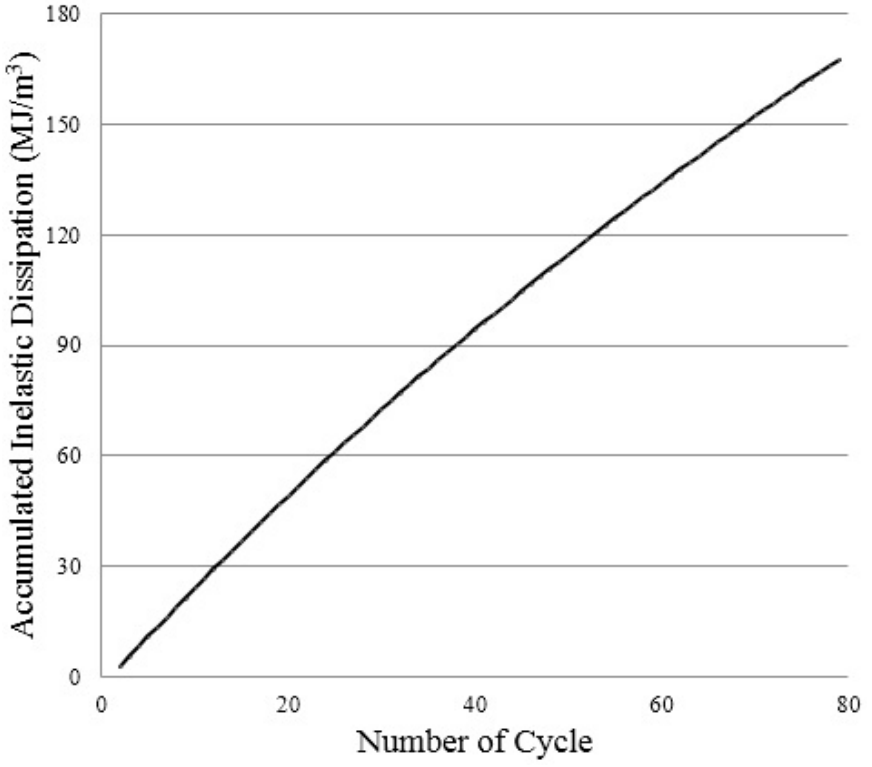

(b) 15-day aged sample at 25°C

Figure 4.6. Accumulated inelastic dissipation vs. number of cycles under different aging conditions during 25°C fatigue cycling.

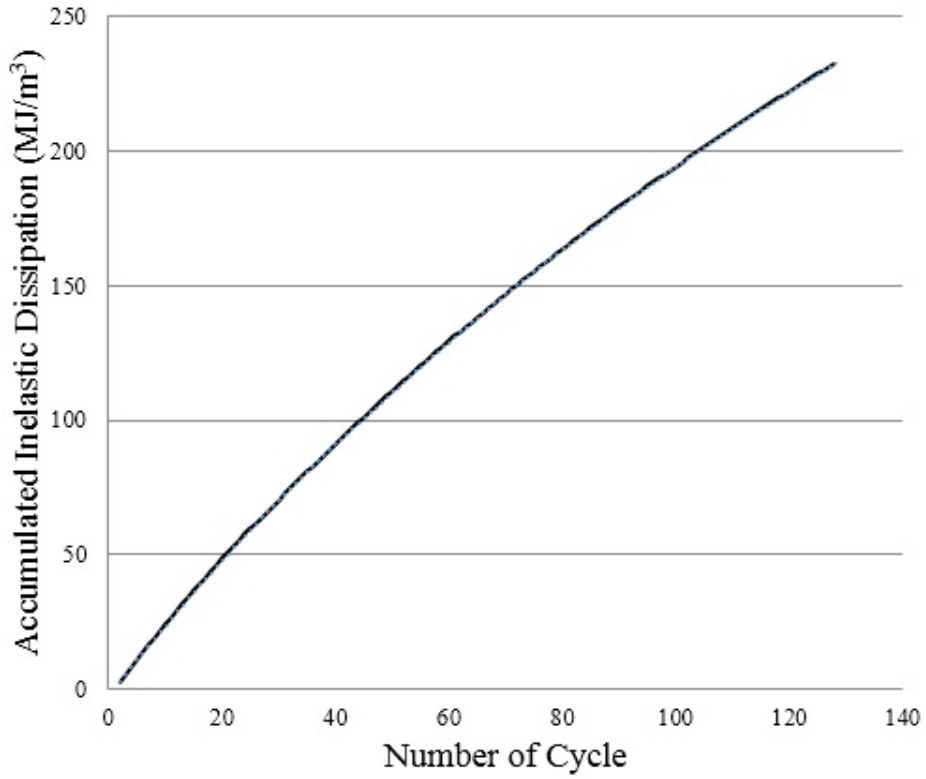

(a) 30-day aged sample at 25°C

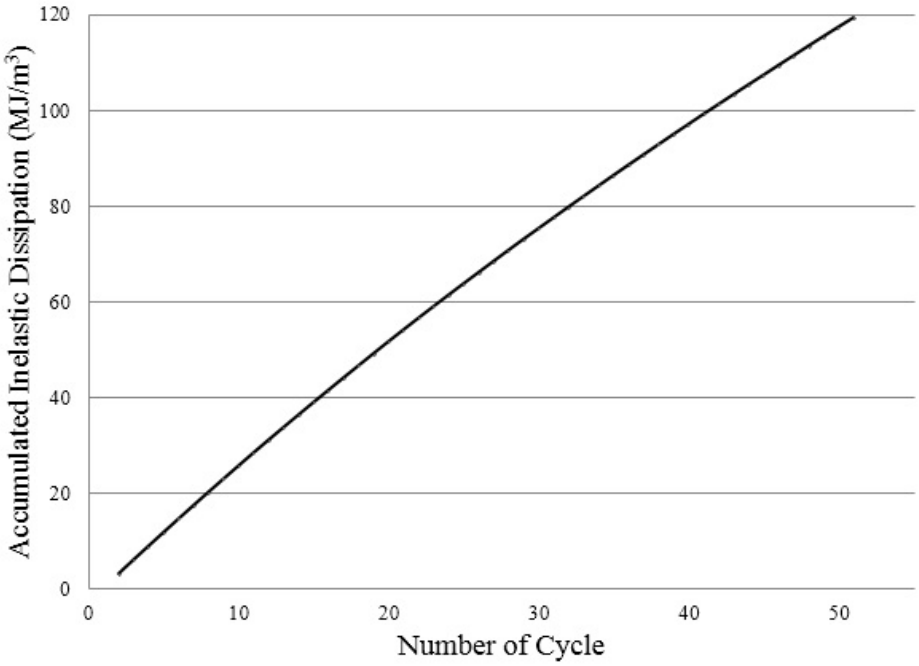

(b) 60-day aged sample at 25°C

Figure 4.7. Accumulated inelastic dissipation vs. number of cycles under different aging conditions during 25°C fatigue cycling.

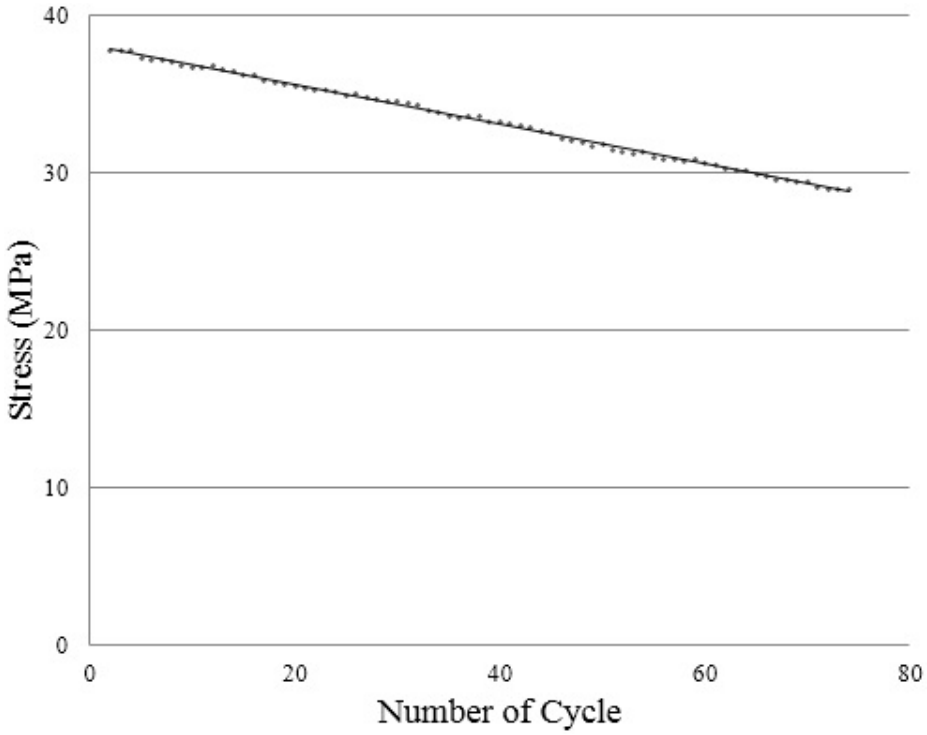

Figure 4.8. Measured stress drop of unaged Sn3.0Ag0.5Cu sample at 25°C.

Table 4.5. The estimated damage accumulation parameters of Sn3.0Ag0.5Cu samples under different aging conditions obtained from 25°C fatigue tests (Unit:mJ/gK).

Aging Day(s)	25C	R^2
0	316	0.991
15	154	0.994
30	143	0.998
60	139	0.997

where S is accumulated entropic dissipation and ρ, is the density of Sn3.0Ag0.5Cu solder alloy, 7400 kg/m^3. If k_ψ is considered as a constant value during experiment, the k_ψ of each test could be extracted by linear fit on Equation (4.4) using the data from the entire test. Figures 4.9 and 4.10 show reasonable linearity between $-\ln(1-D)$ and S under different aging conditions at 25°C, which justifies the extraction of a single k_ψ from linear fit for different pretest aging conditions under this fatigue test condition. For example, in Figure 4.9(a), the slope of fitting line for unaged Sn3.0Ag0.5Cu solder joint at 25°C is 0.427 and k_ψ is calculated as follows:

$$k_\psi = \frac{1}{slope * \rho} = 316\ mJ/gK \tag{4.6}$$

The damage accumulation parameters under different pretest aging conditions at 25°C are summarized in Table 4.5. A larger k_ψ value implies a smaller slope in Figures 4.9 and 4.10. In other words, given a total accumulated dissipation, the accumulated damage is less and therefore a slower fatigue damage is expected. The influence of pretest aging on fatigue behavior is elaborated in Section 5.2.

It is worth mentioning that Equation (3.18) is derived from Equation (3.17) based on an important assumption that the inelastic dissipation rate $\dot{W}_t$ is a constant value. Figure 4.6 and 4.7 show the accumulated inelastic dissipation vs. number of cycles at 25°C tests under different pretest aging conditions. For practical purposes, it is reasonable to assume that inelastic dissipation rate is constant in these 25°C tests.

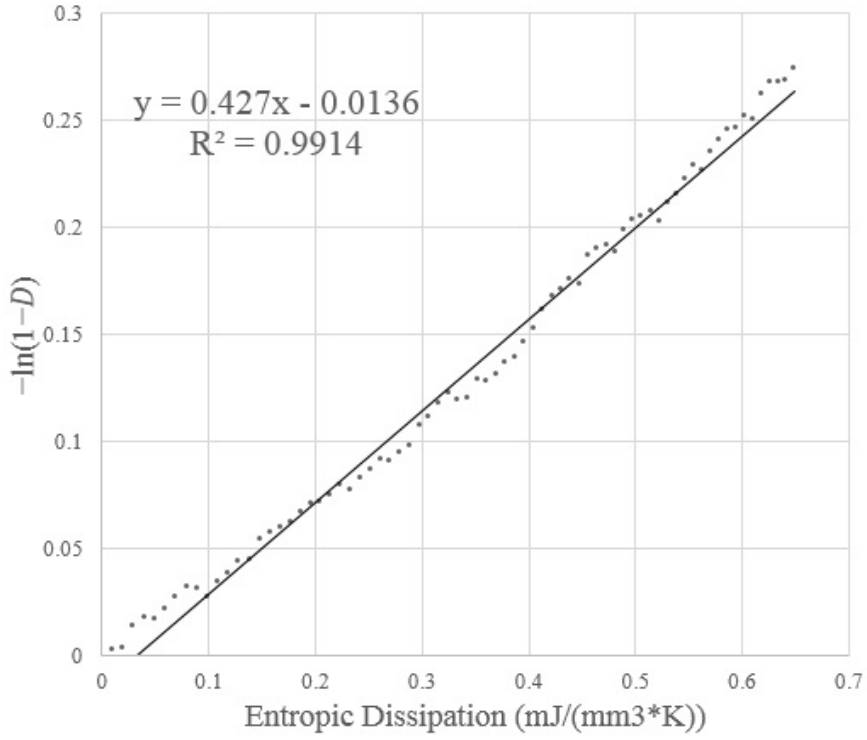

(a) Unaged sample at 25°C

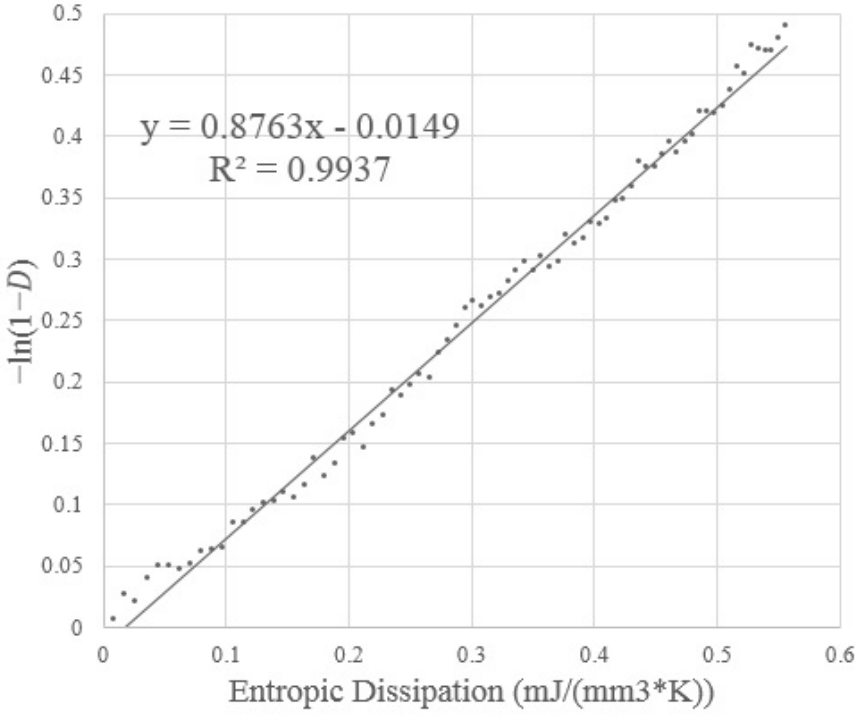

(b) 15-day aged sample at 25°C

Figure 4.9. $-\ln(1-D)$ vs. $\frac{W_t}{T}$ of Sn3.0Ag0.5Cu solder joints during 25°C fatigue tests.

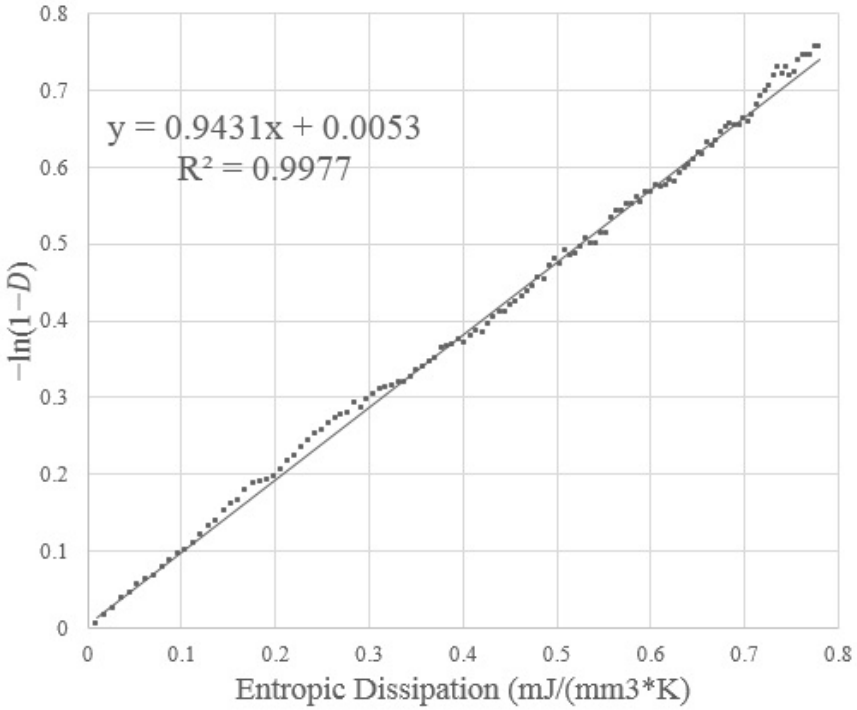

(a) 30-day aged sample at 25°C

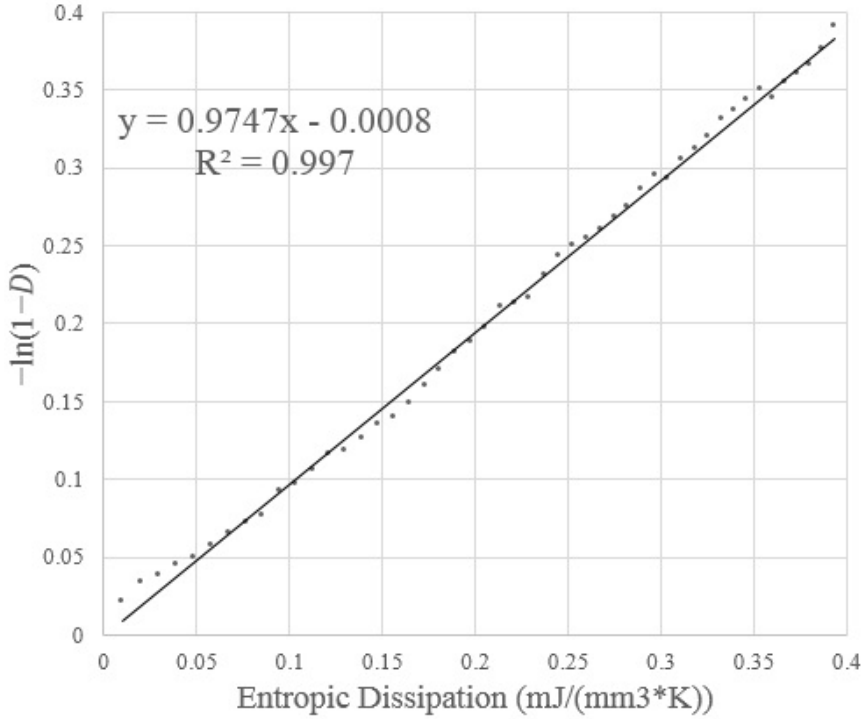

(b) 60-day aged sample at 25°C

Figure 4.10. $-\ln(1-D)$ vs. $\frac{W_t}{T}$ of Sn3.0Ag0.5Cu solder joints during 25°C fatigue tests.

However, in the results of the 100°C fatigue tests shown in Figures 4.11 and 4.12, the constant inelastic dissipation rate assumption does not hold. Figure 4.13 shows the inelastic dissipation at each cycle of 15-day aged sample in 100°C test; the dissipation drops significantly at the beginning of test.

As described earlier, Equation (4.3), the inelastic dissipation consists of two parts: the creep dissipation and the rate-independent plastic dissipation. In Figure 4.13, the creep dissipation makes a significant contribution to the total inelastic dissipation. From Equation (2.1), for a given Z_p, the change of temperature from 25°C to 100°C could greatly increase $\dot{\epsilon}_{ss}$, the minimum creep strain rate and hence the creep dissipation. Since the creep dissipation of each cycle decreases rapidly, the inelastic dissipation decreases as well. Therefore, the constant inelastic dissipation rate assumption is not valid during 100°C fatigue tests and Equation (3.18) should be reconsidered. A new equation relating damage D to accumulated inelastic dissipation W_t needs to be developed. This is carried out below. The accumulated entropy production is as follows:

$$\psi = \frac{W_t}{\rho T} \tag{4.7}$$

where ρ is density and T is temperature, both assumed constant. Based on Figure 4.11 and 4.12, the entropy can be described using a mathematical form

$$\psi(t) = \frac{W_t}{\rho T} = At^B \ (A > 0, 1 > B > 0) \tag{4.8}$$

Taking natural logarithm of the equation one gets:

$$\ln(\psi(t)) = B\ln(t) + \ln(A) \tag{4.9}$$

Through a linear fit to the above equation, the values of the constants A and B was obtained and summarized in Table 4.6.

Next, substituting $\psi(t) = At^B$ into Equation (3.17), one gets:

$$\begin{aligned} D(t_0) &= \int_0^{t_0} f(0) exp(-\int_0^{t_0} \frac{At^B}{k_\psi} dt) d\tau \\ &= \frac{A^{-\frac{1}{B}}}{B} f(0)[\Gamma(\frac{1}{B}, 0) - \Gamma(\frac{1}{B}, \frac{At_0^B}{k_\psi})] \end{aligned} \tag{4.10}$$

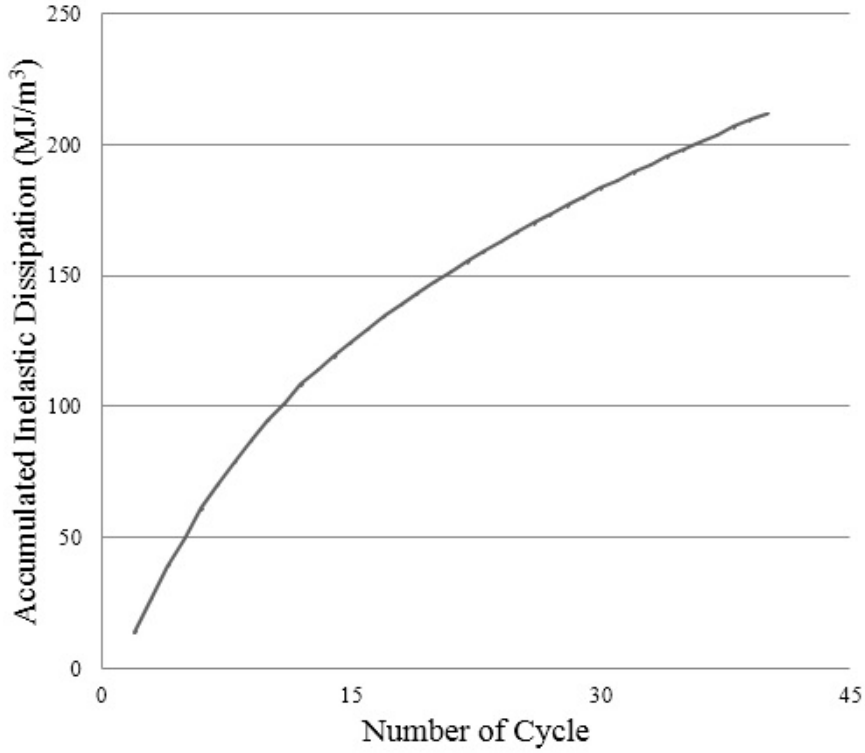

(a) Unaged sample at 100°C

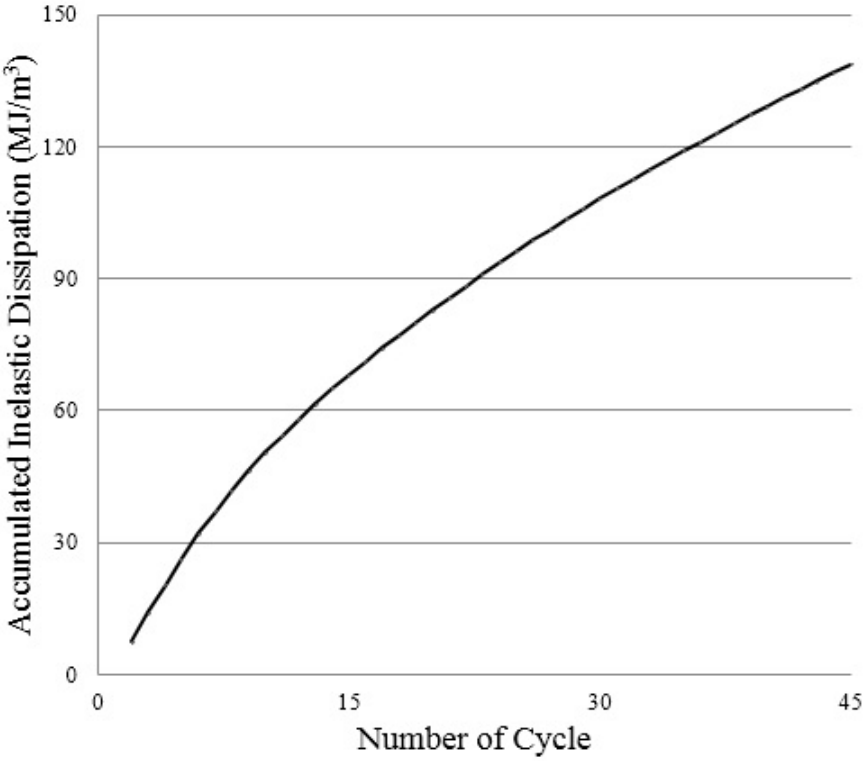

(b) 15-day aged sample at 100°C

Figure 4.11. Accumulated inelastic dissipation vs. number of cycles under different aging conditions during 100°C fatigue cycling.

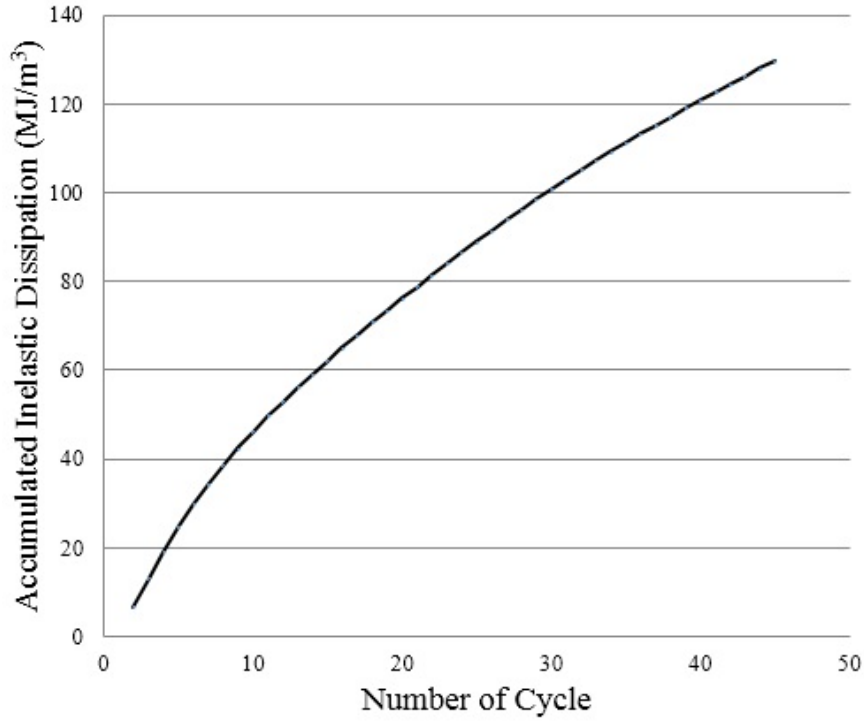

(a) 30-day aged sample at 100°C

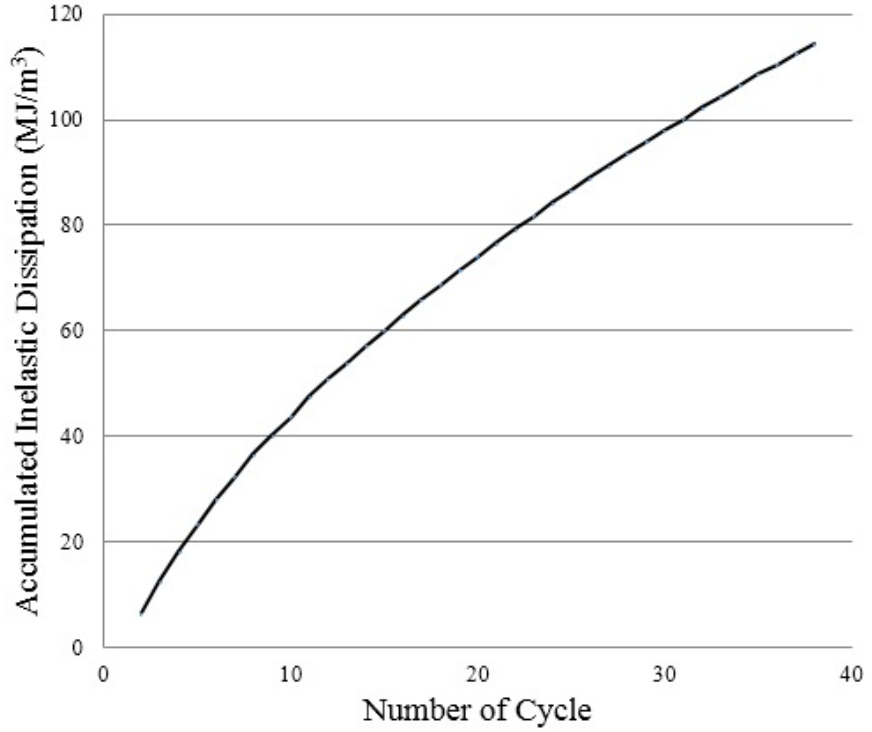

(b) 60-day aged sample at 100°C

Figure 4.12. Accumulated inelastic dissipation vs. number of cycles under different aging conditions during 100°C fatigue cycling.

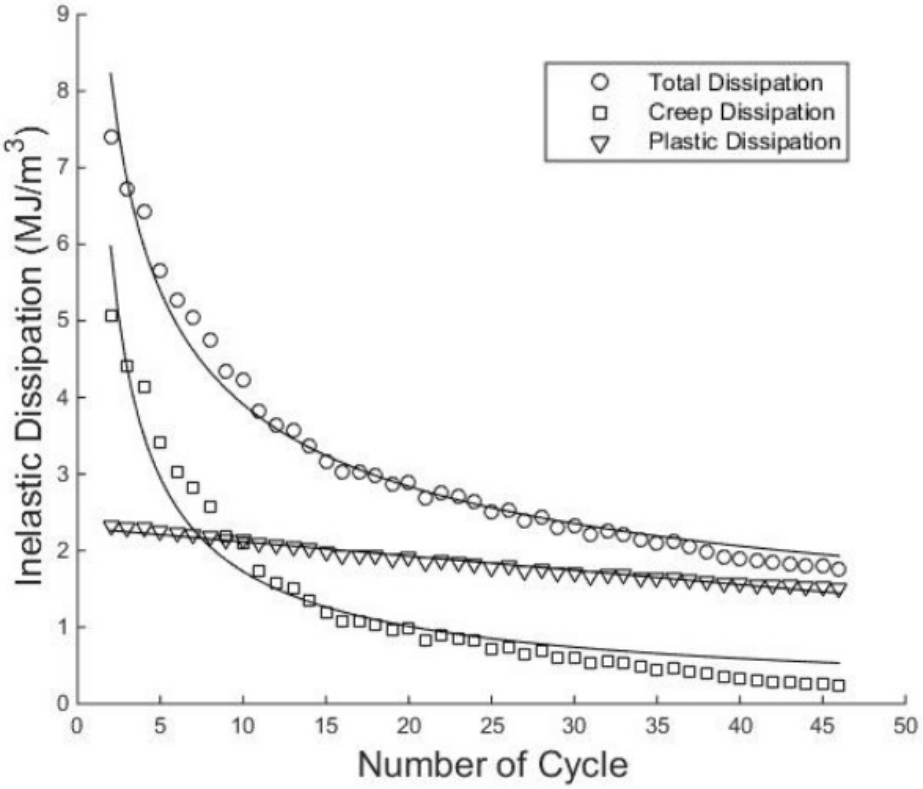

Figure 4.13. The inelastic dissipation at each cycle of 15-day aged sample during 100°C fatigue test.

Table 4.6. The values of constants A and B of $\psi(t) = At^B$ using log-log fit for different pretest aging conditions.

	A	B	R^2
0-day aged	6.74E-06	0.6825	0.984
15-day aged	3.55E-06	0.7060	0.991
30-day aged	3.30E-06	0.7055	0.992
60-day aged	2.82E-06	0.7591	0.995

where $\Gamma(a,b)$ is an incomplete gamma function defined as follows:

$$\Gamma(a,b) = \int_b^\infty t^{a-1}e^{-t}dt \tag{4.11}$$

Again, using $D(\infty) = 1$, one can get $f(0)$ from Equation (4.10). Substituting $f(0)$ back into and further simplifying Equation (4.10), one gets:

$$D(t) = 1 - \frac{\Gamma(\frac{1}{B}, \frac{At^B}{k_\psi})}{\Gamma(\frac{1}{B}, 0)} = 1 - \frac{\Gamma(\frac{1}{B}, \frac{W_t}{\rho T k_\psi})}{\Gamma(\frac{1}{B}, 0)} \tag{4.12}$$

In Equation (4.12), $D(t)$ and W_t are accumulated damage and accumulated inelastic dissipation respectively at the corresponding i^{th} cycle from the beginning of test. So, in each cycle, with a pair of $D(t)$ and W_t determined from experimental data, a k_ψ may be calculated based on Equation (4.12). Figure 4.14 and 4.15 shows the plots of k_ψ values at different cycles during 100°C tests. The k_ψ values change during the 100°C fatigue tests unlike the constant value observed in 25°C fatigue tests under same pretest aging conditions. Further discussion on these plots will be covered in Section 5.3.

4.4 Summary of Fatigue Characterization

Before fatigue characterization, the constitutive model for each pretest aging condition was constructed based on the microstructurally adaptive creep model proposed by Chavali et al. [15] in Chapter 2. Microstructural characterization is a necessary input for the development of the constitutive model. The test method to acquire cyclic fatigue data in this study is similar to that used by Chan et al. and described in Chapter 3. For 25°C cases, the entropic dissipation rate is assumed to be constant and the damage accumulation parameter is extracted using linear fit with the adaptive creep model. However, during fatigue tests at 100°C, the constant inelastic dissipation rate assumption did not hold. A power law form was adopted to empirically fit the 100°C fatigue data to determine the relationship between accumulated entropic dissipation ψ and time t. Using this power law form and MEFM, a new relationship between accumulated damage and accumulated inelastic dissipation was

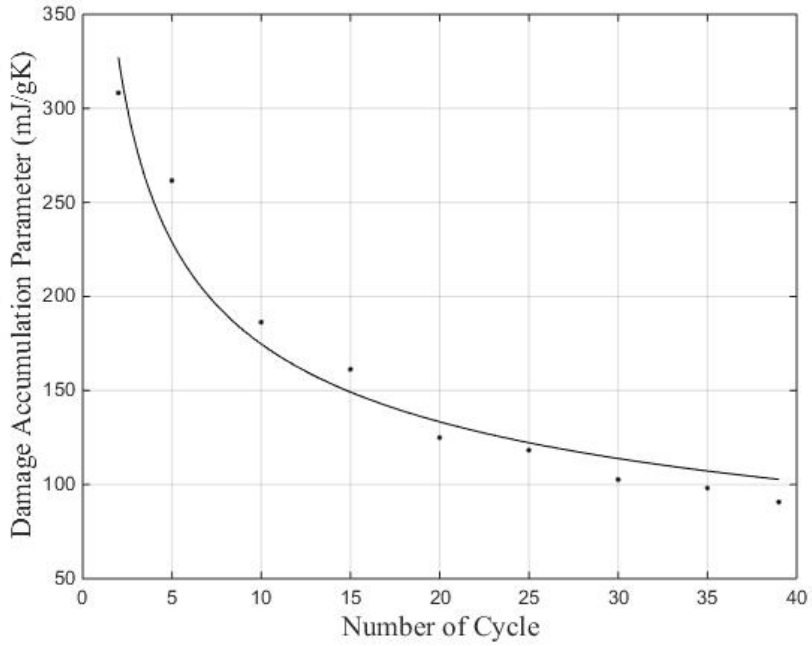

(a) Unaged sample at 100°C

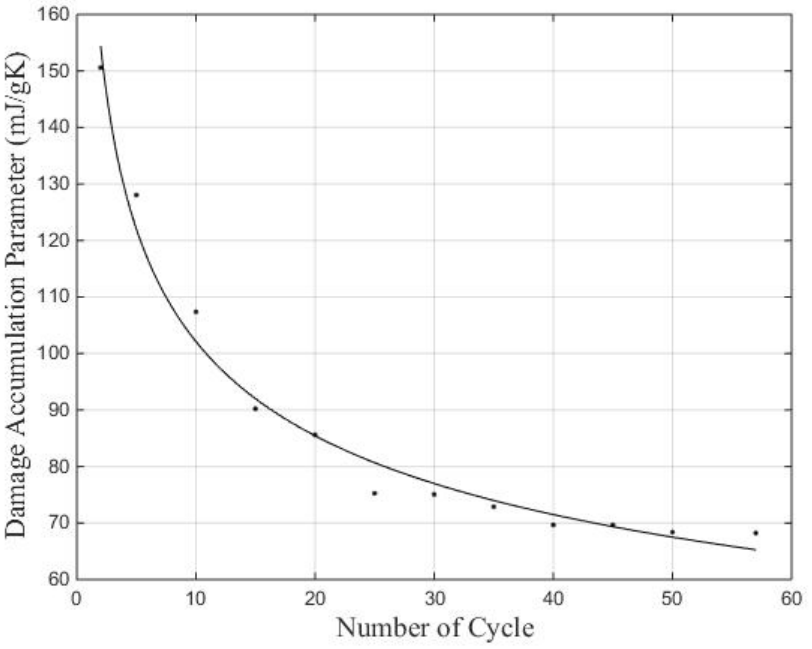

(b) 15-day aged sample at 100°C

Figure 4.14. The damage accumulation parameter k_ψ vs. number of cycles during the 100°C fatigue test.

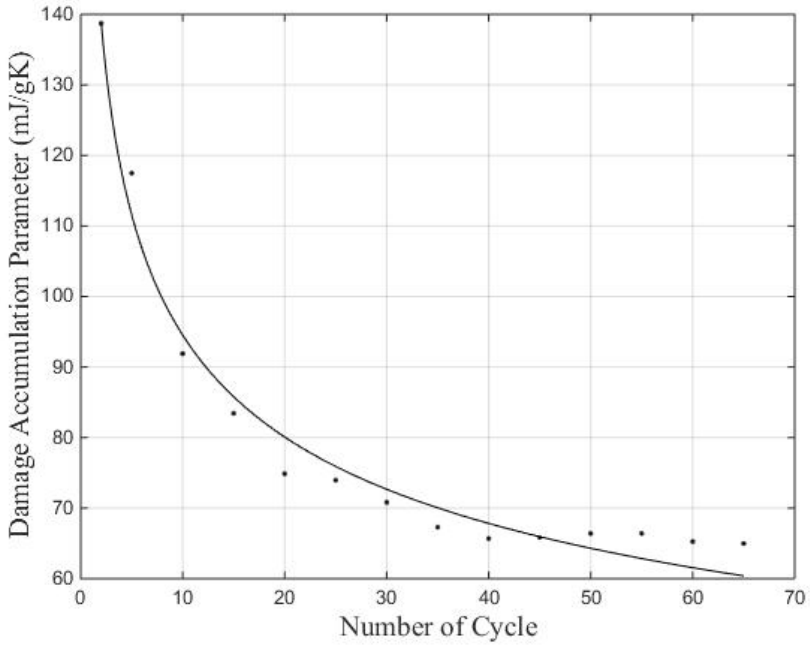

(a) 30-day aged sample at 100°C

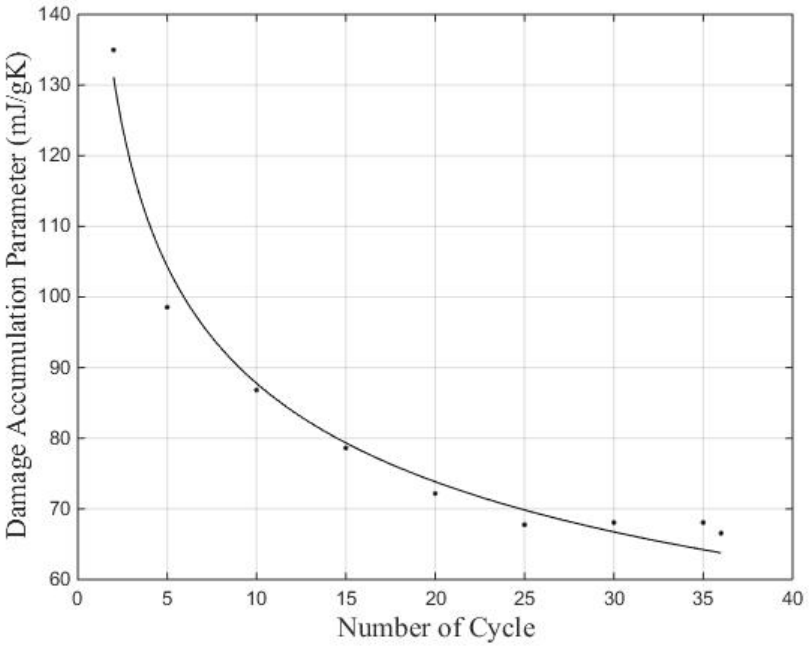

(b) 60-day aged sample at 100°C

Figure 4.15. The damage accumulation parameter vs. number of cycles during the 100°C fatigue test.

derived for 100°C cases, which enables the determination on damage accumulation parameter.

Under the same pretest aging conditions, the estimated damage accumulation parameters from 25°C and 100°C fatigue tests are different. This indicates that continued aging occurs during the fatigue test. In the next chapter, the pretest aging and in-test aging will be described in terms of static aging and dynamic aging. The effect of static aging and dynamic aging on fatigue behavior of Sn3.0Ag0.5Cu solder joints will be examined.

5. INFLUENCE OF AGING ON FATIGUE BEHAVIOR OF SN3.0AG0.5CU SOLDER JOINTS

5.1 Review: Effect of Aging on Mechanical Response of SnAgCu Alloys

Existing studies have revealed that aging could cause degradation of mechanical properties of SnAgCu alloys. Hasnine et al. [33] explored the influence of aging on Sn3.0Ag0.5Cu solder joints on Plastic Ball Grid Array (PBGA) assemblies by nanoindentation. Mechanical properties including elastic modulus, hardness and yield stress were characterized as a function of aging. By performing tensile and creep tests on samples with different mixture ratios of Sn3.0Ag0.5Cu and 63Sn37Pb, Zhang et al. [2] studied the mechanical properties under different aging conditions. Dutta et al. [34] showed that the coarsening caused by isothermal and thermomechanical cycling (TMC) could increase the fracture toughness in Mode I because of the softening effect of material. Venkatadri et al. [35] characterized the aging state of solder joints in terms of the decrease of shear strength, shear fatigue resistance and micro hardness at room temperature for Sn1.0Ag0.5Cu, Sn3.0Ag0.5Cu and Sn4.0Ag0.5Cu alloys.

5.2 Effect of Static Aging on Fatigue Behavior of Sn3.0Ag0.5Cu Solder Joints

Static aging is defined here as the aging caused by temperature alone, when sample is not subject to stress, such as the pretest aging conditions in this study. Dynamic aging is said to occur when sample is subject to stress at a specified temperature. Therefore, in-test aging includes the effects from both dynamic aging and static aging.

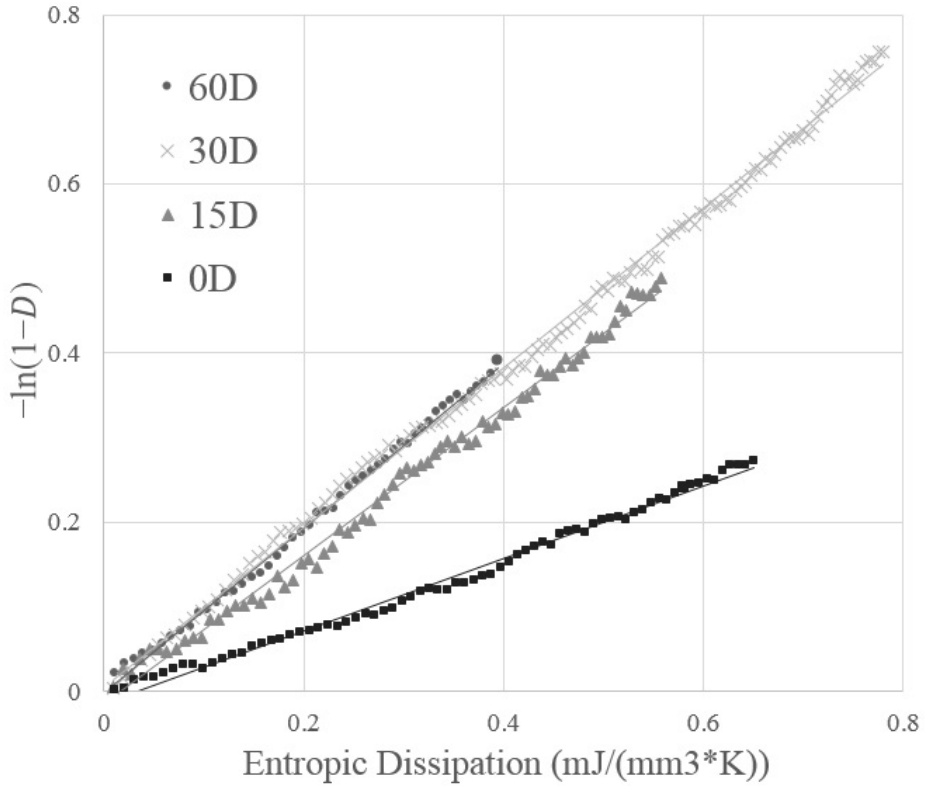

Figure 5.1. $-\ln(1-D)$ vs. $\frac{W_t}{T}$ of Sn3.0Ag0.5Cu solder joints under different aging conditions in 25°C tests.

In Section 4.3, the experimental data from 25°C tests is plotted based on Equation (4.4) as follows:

$$-\ln(1-D) = \frac{1}{\rho k_\psi}\frac{W_t}{T}$$

Figure 5.1 shows reasonable linearity between $-\ln(1-D)$ and entropic dissipation $\frac{W_t}{T}$, which indicates that the damage accumulation parameter k_ψ didn't change significantly during 25°C tests because k_ψ is inversely proportional to the slope in Figure 5.1. Therefore, we can conclude that the in-test aging during 25°C fatigue tests is relatively limited and therefore, only the pretest aging, namely, different static aging conditions affect the fatigue behavior of samples. Thus, using 25°C tests, one can study the influence of static aging on fatigue behavior.

Since a constant k_ψ is a reasonable assumption, a linear fit was adopted to determine the damage accumulation parameters k_ψ under different static aging conditions.

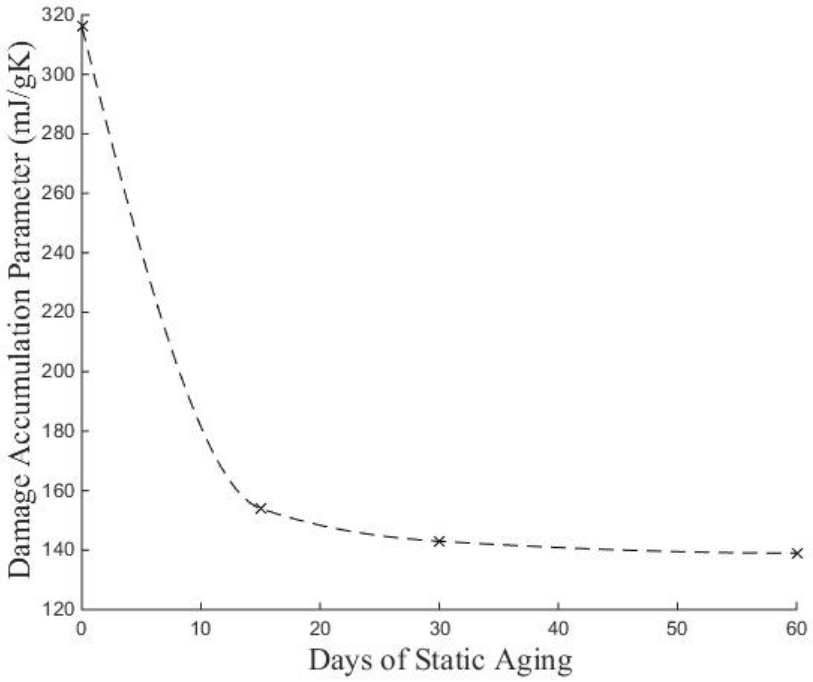

Figure 5.2. Damage accumulation parameters from 25°C fatigue tests vs. days of static aging of test samples.

The relationship between k_ψ and the number of static aging days is shown in Figure 5.2. As the time of static aging becomes longer, the damage accumulation parameter value decreases. It decreases significantly from 0 day (unaged) to 15 days but changes very slowly from 15 days to 60 days. Similar set of experiments were performed by Tucker et al. [14] and an almost constant k_ψ was found from 10-day to 150-day aged samples. Given the timescale of pretest aging in this study (up to 60 days), a static-aged k_ψ limit of Sn3.0Ag0.5Cu alloy exists and it is close to the k_ψ values of 15/30/60-day aged samples. This concept would be utilized in the analysis of dynamic aging in the next section.

Prior to tests, the samples were placed in a thermal chamber at 125°C for static aging. At such a high temperature, faster diffusion is expected and as a result, $Ag3Sn$ particles become coarser and disperse, while the primary-Sn cell size grows larger. Referring to Figure 4.1 and 4.2, static aging could hasten microstructural

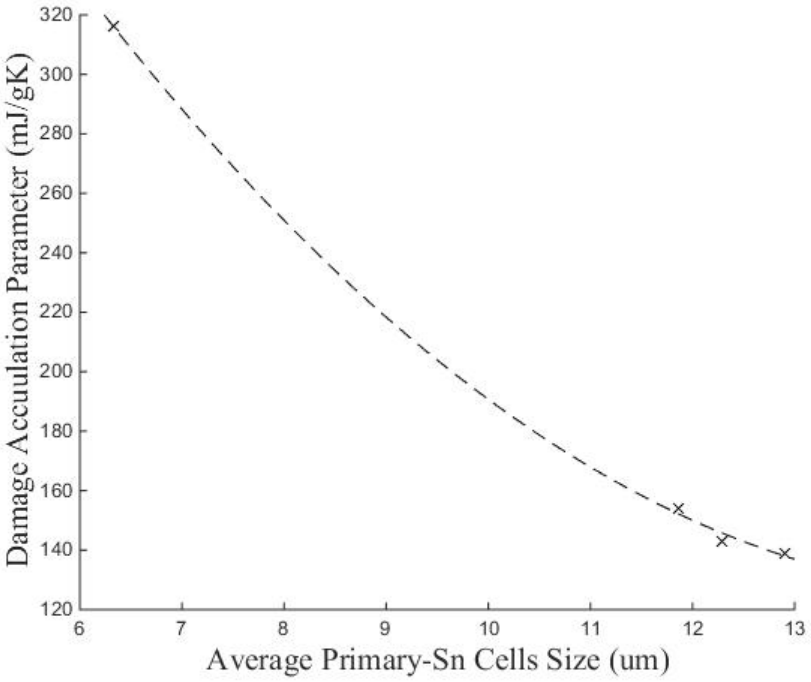

Figure 5.3. Damage accumulation parameter value from 25°C fatigue tests on statically aged samples vs. average primary-Sn cell size of samples.

evolution of SnAgCu alloys and change the mechanical behavior. Faster primary creep behavior and lower resistance to fatigue fracture are expected. Figure 5.3 presents the relationship between damage accumulation parameter k_ψ and the average primary-Sn cells size $\bar{\eta}$. With a larger average primary-Sn cell size due to longer static aging, a smaller damage accumulation parameter is anticipated, which implies a faster fatigue crack propagation. Therefore, the microstructure of SnAgCu alloys has a significant influence on the damage accumulation parameter.

5.3 Effect of Dynamic Aging on Fatigue Behavior of Sn3.0Ag0.5Cu Solder Joints

In Section 4.3, Equation (4.12) relating accumulated damage $D(t)$ and accumulated inelastic dissipation W_t was derived using the concepts of MEFM for 100°C fatigue tests since in these tests, the dissipation rate was no longer a constant:

$$D(t) = 1 - \frac{\Gamma(\frac{1}{B}, \frac{At^B}{k_\psi})}{\Gamma(\frac{1}{B}, 0)} = 1 - \frac{\Gamma(\frac{1}{B}, \frac{W_t}{\rho T k_\psi})}{\Gamma(\frac{1}{B}, 0)}$$

The damage accumulation parameters k_ψ were calculated based on the above equation and plotted against number of cycles in Figure 4.14 and 4.15. As we can see, the estimated k_ψ values decrease as the tests continue. This indicates in-test aging is not negligible and needs to be considered during high temperature fatigue tests.

Before we further discuss in-test aging, the meaning of k_ψ values from 100°C cases needs to be examined and compared to that in 25°C tests. In Maximum Entropy Fracture Model, the damage accumulation parameter k_ψ is a measure of fatigue damage accumulation rate. A lower k_ψ value indicates a greater accumulated damage is achieved given a specific generated accumulated inelastic dissipation, which means faster fatigue process. For each 25°C test, a single k_ψ value was extracted from the entire test data by linear fit. While in 100°C tests, the k_ψ value is calculated from each pair of accumulated damage and inelastic dissipation data. Instead, using $\bar{k}_n$ for 100°C cases would be easier to understand. $\bar{k}_n$ is the effective average damage accumulation parameter from the beginning of test to the n^{th} cycle. That means $\bar{k}_n$ could accurately predict the accumulated damage at n^{th} cycle given the accumulated inelastic dissipation.

The $\bar{k}_n$ at the 1^{st} cycle of 100°C tests are compared with k_ψ from 25°C tests in Table 5.1. Under same static aging conditions, the damage accumulation parameters from 100°C and 25°C tests are nearly identical. This indicates that at the beginning of 100°C tests, the samples will accumulate fatigue at almost at the same rate as that in 25°C tests, which further validates the observation that in-test aging is negligible in 25°C tests and their k_ψ values are only dependent on static aging.

Table 5.1. Comparision between k_ψ of 25°C tests and $\bar{k}_n$ at the 1^{st} cycle of 100°C tests. k_ψ of 25°C tests are deemed accurate.

Aging Days(125C)	25C	100C	Error(%)
0D	316	308	2.5
15D	154	151	1.9
30D	143	139	2.8
60D	139	135	2.9

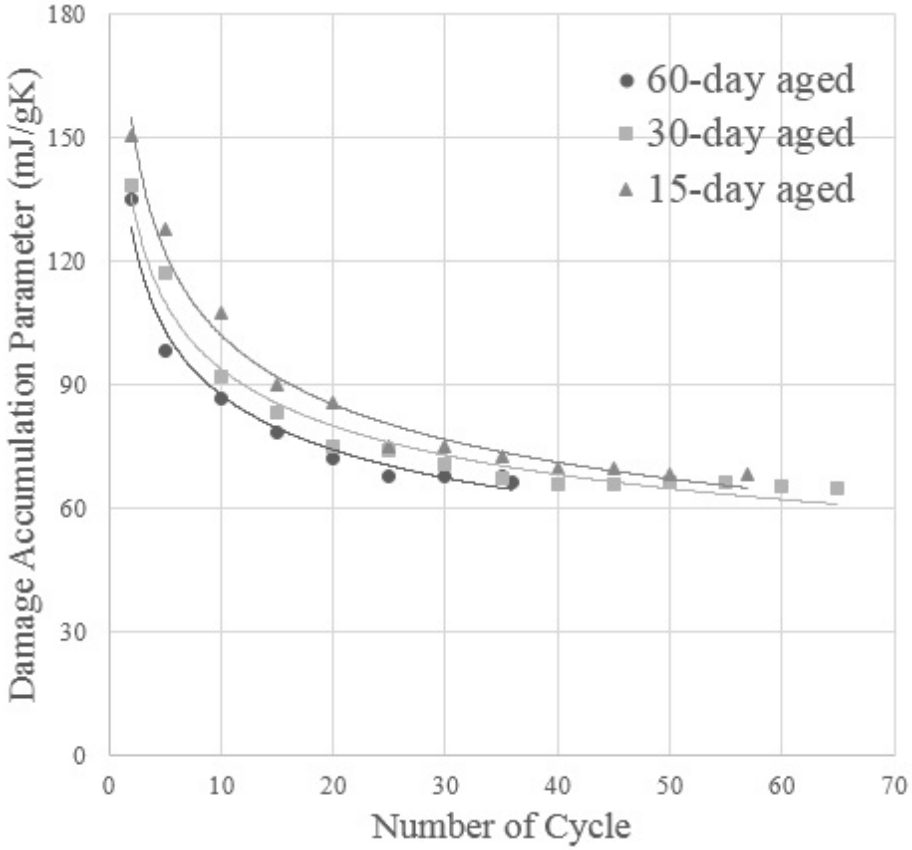

Figure 5.4. $\bar{k}_n$ vs. number of cycles for 15/30/60-day aged samples during 100°C fatigue tests.

In Figure 5.4, the $\bar{k}_n$ values of 15/30/60-day aged samples in 100°C tests are plotted against number of cycles. Their $\bar{k}_n$ values steadily decrease and reach a near constant value of around 70 mJ/gK. Table 5.2 summarizes the time t_s when $\bar{k}_n$ becomes stable and the corresponding $\bar{k}_n$ values at that time of aged samples in 100°C tests. t_s is the time when the derivative of the fitted curve (in $y = ax^b$ form) in Figure 5.4 drops to 1% of its value at the end of the 1^{st} cycle. With longer pretest aging, the microstructure evolves to stable state in a shorter period. The stable $\bar{k}_n$ values of aged samples are very close in value, ranging from 67 mJ/gK to 71 mJ/gK. This indicates that under the effect of in-test aging, the samples' microstructure evolves and gradually becomes stable at similar microstructural states.

Table 5.2. The time t_s when $\bar{k}_n$ becomes stable at $\bar{k}_s$ of aged samples in 100°C tests.

	t_s $Hour$	$\overline{k_s}$ mJ/gK
15-day aged	32.3	69
30-day aged	25.4	71
60-day aged	24.3	67

As mentioned in Section 5.2, the in-test aging has both static aging and dynamic aging. The static aging portion of in-test aging in 100°C tests with aged samples is very limited. In Figure 5.2, the k_ψ values of 15/30/60-day aged samples are close to static-aged k_ψ values. Besides, the duration of experiment is much shorter than pretest aging. As a result, in 100°C tests with aged samples, the dynamic aging is the dominant one during in-test aging. Compared to static aging, dynamic aging could further evolve the microstructure of even the fully static-aged samples and decrease $\bar{k}_n$ down to a constant value. Thus, under the effect of dynamic aging, a faster fatigue fracture is anticipated during 100°C tests.

5.4 Summary

In this chapter, the deterioration of mechanical properties of SnAgCu alloys caused by aging was reviewed at the beginning. Different techniques to characterize mechanical properties were mentioned as well. The concepts of static aging and dynamic aging were clarified. From 25°C tests, we can study the effect of static aging on fatigue behavior because the in-test aging is very limited. By establishing the relationship between k_ψ and the average primary-Sn cells size $\bar{\eta}$, the influence of microstructure on the damage accumulation parameter was revealed. In 100°C tests, a new relationship between accumulated damage and accumulated inelastic dissipation was derived and $\bar{k}_n$ was differentiated from k_ψ of 25°C fatigue tests. Under the effect of in-test aging, $\bar{k}_n$ decreases as experiment continues and finally stabilizes at a constant value, which indicates that the microstructure evolves to a fully aged state. Finally we argue that for the aged sample tests at 100°C, the static aging is negligible and therefore dynamic aging could further age a fully static-aged sample and degrade the fatigue behavior of SnAgCu alloys until the microstructure becomes fully stabilized.

6. SUMMARY AND FUTURE WORK

6.1 Summary

In order to study the influence of pretest aging and in-test aging on fatigue behavior of Sn3.0Ag0.5Cu alloys, isothermal cyclical fatigue tests were conducted on Sn3.0Ag0.5Cu solder joints using custom-built equipment under different aging conditions. Experimental data was analyzed using the Maximum Entropy Fracture Model (MEFM) as the failure model and Microstructurally Adaptive Creep Model as the constitutive model. The concepts of static aging and dynamic aging were introduced to describe pretest aging and in-test aging. For 25°C tests, a single damage accumulation parameter k_ψ was extracted from each experiment. Upon static aging, fatigue behavior of Sn3.0Ag0.5Cu alloy degrades because of microstructural evolution and a single value of k_ψ was obtained. In 100°C tests, due to dynamic aging, no single value of k_ψ describes data over the entire test. Therefore, $\bar{k_n}$ was calculated and plotted against number of cycles, which captures the effect of dynamic aging, and asymptotically reaches a steady value. Thus, the higher temperature fatigue tests cause considerable in-test dynamic aging further degrading fatigue behavior relative to fatigue tests at 25°C.

6.2 Future Work

In Section 5.2, the 25°C tests show the influence of static aging on the damage accumulation parameter k_ψ. In order to fully characterize the relationship between k_ψ and the average primary-Sn cell size $\bar{\eta}$, more experiments at 25°C with different pretest aging conditions are necessary, especially at those aged over 0 to 15-day period.

Fatigue tests at different temperatures with fully static-aged samples are required to better understand and build a dynamic aging model. Cross sectioning fatigue

tested samples and characterizing their microstructural features should be adopted to build an microstructural evolution model as a function of thermal and strain history based on this experiment method.

Finally, this study should be extended to other SnAgCu alloys.

LIST OF REFERENCES

LIST OF REFERENCES

[1] D.K. Chan. *A Maximum Entropy Fracture Model for Low and High Strain-rate Fracture in SnAgCu Alloys*. PhD thesis, Purdue University, 2012.

[2] J. Zhang, Z. Hai, S. Thirugnanasambandam, J.L. Evans, M.J. Bozack, Y. Zhang, and J.C. Suhling. Thermal Aging Effects on the Thermal Cycling Reliability of Lead-Free Fine Pitch Packages. *Transactions on Components, Packaging and Manufacturing Technology*, 3(8), 2013.

[3] M. Motalab, M. Mustafa, J.C. Suhling, J. Zhang, J. Evans, M.J. Bozack, and P. Lall. Correlation of Reliability Models Including Aging Effects with Thermal Cycling Reliability Data. *Electronic Component and Technology Conference*, pages 986–1004, May 2013.

[4] T. Lee, H. Ma, K. Liu, and J. Xue. Impact of Isothermal Aging on Long-Term Reliability of Fine-Pitch Ball Grid Array Packages with Sn-Ag-Cu Solder Interconnects: Surface Finish Effects. *Journal of Electronic Materials*, 39(12), 2010.

[5] T. Lee, B. Zhou, and T.R. Bieler. Impact of Isothermal Aging and Sn Grain Orientation on the Long-Term Reliability of Wafer-Level Chip-Scale Package Sn-Ag-Cu Solder Interconnects. *IEEE*, 2(3), 2012.

[6] R. Coyle, M. Reid, C. Ryan, R. Popowich, P. Read, D. Fleming, M. Collins, J. Punch, and I. Chatterji. The Influence of the Pb-free Solder Alloy Composition and Processing Parameters on Thermal Fatigue Performance of a Ceramic Chip Resistor. *IEEE*, pages 423–430, 2009.

[7] A. Schubert, R. Dudek, E. Auerswald, A. Gollhardt, B. Michel, and H. Reichel. Fatigue Life Models for snAgCu and SnPb Solder Joints Evaluated by Experiments and Simulations. *IEEE Electronic Components and Technology Conference*, pages 603–610, 2003.

[8] A. Syed. Updated Life Prediction Models for Solder Joints with Removal of Modeling Assumptions and Effect of Constitutive Equations. *EuroSimE Conference*, pages 1–9, 2006.

[9] Q. Zhang, A. Dasgupta, and P. Haswell. Viscoplastic Constitutive Properties and Energy-Partitioning Model of Lead-Free Sn3.9Ag0.6Cu Solder Alloy. *IEEE Electronic Components and Technology Conference*, pages 1862–1868, 2003.

[10] H. Tang and C. Basaran. A Damage Mechanics-Based Fatigue Life Prediction Model for Solder Joints. *Journal of Electronic Packaging*, 125:120–125.

[11] W. Lee, L.T. Nguyen, and G.S. Selvaduray. Solder Joint Fatigue Models: Review and Applicability to Chip Scale Packages. *Microelectronics Reliability*, 40:231–244, 2000.

[12] D. Bhate, K. Mysore, and G. Subbarayan. An Information Theoretic Argument on the Nature of Damage Accumulation in Solids. *Mechanics of Advanced Materials and Structures*, 2012.

[13] D. Chan, G. Subbarayan, and L. Nguyen. Maximum-Entropy Principle for Modeling Damage and Fracture in Solder Joints. *Journal of Electronic Materials*, 41(2):398–411, 2011.

[14] J.P. Tucker. *Microstructural Effects on Constitutive and Fatigue Fracture Behavior of SnAgCu Solder*. PhD thesis, Purdue University, 2012.

[15] S.C. Chavali. *Diffusion Driven Microstructural Evolution and Its Effect on Mechanical Behavior of SnAgCu Solder Alloys*. PhD thesis, Purdue University, 2012.

[16] Q. Xiao, H.J. Bailey, and W.D. Armstrong. Aging Effects on Microstructure and Tensile Property of Sn3.9Ag0.6Cu Solder Alloy. *Journal of Electronic Packaging*, 126:208–212, 2004.

[17] J.C. Suhling, P. Lall, and M.J. Bozack. The Effects of Aging Temperature on SAC Solder Joint Material Behavior and Reliability. 58^th *Electronic Components and Technology Conference*, pages 99–112, May 2008.

[18] D. Bhate, D. Chan, G. Subbarayan, T.C. Chiu, V. Gupta, and D.R. Edwards. Constitutive Behavior of Sn3.8Ag0.7Cu and Sn1.0Ag0.5Cu Alloys at Creep and Low Strain Rate Regimes. *IEEE Transactions on Components and Packaging Technologies*, 31(3):622–633, 2008.

[19] C. Zener and J. H. Hollomon. Effect of Strain Rate Upon Plastic Flow of Steel. *Journal of Applied Physics*, 15(1):106–114, 1944.

[20] G.A. Webster, A.P.D. Cox, and J.E. Dorn. A Relationship between Transient and Steady-State Creep at Elevated Temperature. *Metal Science*, 3(1):221–225, 1969.

[21] K.E. Amin, A.K. Mukherjee, and J.E. Dorn. A Universal Law for High-Temperature Diffusion Controlled Transient Creep. *Journal of the Mechanics and Physics of Solids*, 18(6):413–426, 1970.

[22] H.J. Frost and M.F. Ashby. *Deformatoin Mechanism Maps-The Plasticity and Creep of Metals and Ceramics*. Pergamon Press, 1982.

[23] J.J. Jonas, C.M. Seller, and W.J. McTegart. Strength and Structure Under Hot Working Conditions. *metals Review*, 14(1), 1969.

[24] L. Coffin. Predictive Parameters and Their Application to High-Temperature, Low-cycle Fatigue. *Science*, 1969.

[25] S.S. Manson. Interfaces between fatigue, creep, and fracture. *Int J Fract*, 2(1), March 1966.

[26] P.C. Paris, M.P. Gomez, and W.E. Anderson. A Rational Theory of Fatigue. *The Trend in Engineering*, 13(1):9–14, 1961.

[27] V. Stolkarts, L.M. Keer, and M.E. Fine. Damage Evolution Governed by Microcrack Nucleation with Application to the fatigue of 63Sn-37Pb Solder. *Journal of the Mechanics and Physics of Solids*, 417(12):2451–2468, 1999.

[28] C. Shannon. A Mathematical Theory of Communication. *The Bell System Technical Journal*, 27(7):379–423, 1948.

[29] J. Aizenberg, J.C. Weaver, M.S. Thanawala, V.C. Sundar, D.E. Morse, and P. Fratzl. Skeleton of Euplectella sp.:Structural Hierarchy from the Nanoscale to the Macroscale. *Science*, 309(5732):275–278, May 2005.

[30] E.T. Jaynes. Information Theory and Statistical Mechanics. *Phys. Rev.*, 106(4):620–630, May 1957.

[31] R. Bowley and M. Sanchez. *Introductory Statistical Mechanics*. Oxford University Press, USA, second edition, 2000.

[32] K. Mysore, G. Subbarayan, V. Gupta, and R. Zhang. Constitutive and Aging Behavior of Sn3.0Ag0.5Cu Solder Alloy. *IEEE Transactions on Electronics Packaging Manufacturing*, 32(4).

[33] M. Hasnine, M. Mustafa, J.C. Suhling, B.C. Prorok, M.J. Bozack, and P. Lall. Characterization of Aging Effects in Lead Free Solder Joints Using Nanoindentation. *Electronic Components and Technology Conference*, 2013.

[34] I. Dutta, P. Kummar, and G. Subbarayan. Microstructural Coarsening in Sn-Ag-based Solders and Its Effects on Mechanical Properties. *The Journal of The Minerals, Metals and Materials Society*, 61(6), 2009.

[35] V. Venkatadri, L. Yin, Y. Xing, E. Cotts, K. Srihari, and P. Borgesen. Accelerating the Effects of Aging on Reliability of Lead Free Solder Joints in a Quantitative Fashion. *Electronic Components and Technology Conference*, 2009.